UNIVERSITY OF CALIFORNIA
SANTA CRUZ

# COHERENT SURFACE ACOUSTIC WAVE REFLECTION VIA MICROFLUIDIC PHONONIC CRYSTAL DEVICES

A thesis submitted in partial satisfaction of the

requirements for the degree of

MASTER OF SCIENCE

in

ELECTRICAL ENGINEERING

by

**Sierra Jade Catelani**

December 2017

The Thesis of Sierra Catelani is approved:

_____
Professor Ahmet Ali Yanik, Chair

_____
Professor Marco Rolandi

_____
Professor Holger Schmidt

_____
Tyrus Miller
Vice Provost and Dean of Graduate Studies

# Table of Contents

# List of Figures

# Abstract

Coherent Surface Acoustic Wave Reflection via Microfluidic Phononic Crystal Devices

By Sierra Catelani

The integration of surface acoustic wave (SAW) technology with Lab-on-a-Chip (LOC) devices has enabled powerful acoustic mechanisms for cell sorting, cell deflection, and other types of manipulation of biological specimen. Their control can be further enhanced and specialized with the integration of phononic crystals, which are materials designed to have phononic bandgaps to control the propagation of acoustic waves through a substrate. While many methods of designing phononic crystals require fabrication techniques that alter the surface topology with pillar or hole arrays, our electropoling technique creates a completely monolithic substrate. Electropoling involves using a strong electric field to reverse the domains of a piezoelectric substrate in a periodic pattern to generate a phononic bandgap. The technique is both simple and allows for compatibility with microfluidic components. By integrating phononic crystal substrates into a LOC device, we can enable a new degree of control to SAW particle manipulation. Here we demonstrate the use of phononic crystals to reflect SAWs in order to generate standing SAW fields. Particle focusing experiments are performed to observe the standing wave pattern. This is a novel demonstration of utilizing reflecting phononic energy towards a functional device, as well as integration of phononic crystal technology into a microfluidic system device.

# Acknowledgements

I would like thank to those in my lab who offered their time to guide me with my research, and opened new opportunities for me to explore the vast amount of topics touched in our lab. Much of the foundation of this project was provided by my colleague Xiangchao "Jude" Zhu's previous work in acoustofluidics. Jude gave me a great deal of guidance throughout this project, and spent countless hours with me discussing literature and conducting experiments. Thank you as well to Yixiang "Louis" Li, who I have spent both frustrating and rewarding days in the cleanroom as we struggled and succeeded to learn complicated fabricated processes together. Louis was also the main force in running simulations for this project. The undergraduate who assisted me with my research, Jose Fuentes, dedicated significant time and effort to this project enthusiastically and helped me develop the hardware for the electropoling setup. My lab mates Imran Hossain and Ahsan Habib also offered a great deal of assistance to me as I navigated my way as a new graduate student. I also want to thank Dr. Ahmet Ali Yanik for giving me the opportunity to conduct this research and providing me the resources and support to make this project successful.

# Chapter 1: Introduction and Background

## 1.1 Motivation

The harnessing of electronic and photonic energy has caused an incredible expanse of technology. Through the progression of the 20th century, scientists and engineers studied these technologies extensively in order to develop control over electrons and photons. In a similar manner, scientists have recently been looking at methods to control another elementary particle: the phonon. The phonon is a quantum particle that represents a single lattice vibration. While not as prevalent as electronic and photonic technology, phonons are responsible for the transmission of sound, acoustic vibrations, and heat. [25] The last two decades has brought a growing field of research focused on developing materials that manipulate the propagation of phonons. A key component of this research effort is the complete phononic bandgap, which is a range of acoustic frequencies that are not able to propagate through the phononic crystal. This technology has already shown some very powerful applications, including thermal devices with controllable thermal conductivity, acoustic diodes which allow acoustic energy to only move in one direction, and optomechanical devices which couple optical energy to mechanical vibrations [17].

One particular application of great interest is designing phononic crystals to control how surface acoustic waves (SAWs) propagate on the surface of a material [23]. Manipulation of SAWs is an important field of study, as SAW based devices

have been used widely for their signal processing ability in high-frequency electronics, mainly in the telecommunications industry, and have been adapted for use in a variety of sensors [22, 34]. They are also used in SAW lab-on-a-chip technology, specifically SAW microfluidic devices which use acoustic forces to enable a variety of fluid actuation and particle manipulation methods [12]. SAW-based particle manipulation is very powerful, as the acoustic force is dependent on the physical parameters of the particles, including size, density, compressibility, and shape [31, 33]. This has important applications in the realm of biology, as SAWs enable selective sorting of biological specimen of different sizes [31]. In this way, SAW microfluidic devices can be used to separate very small, rare cells such as circulating tumor cells (CTCs) or exosomes, which has been used for disease diagnostics [33].

Most SAW-based LOC devices use one of two common architectures, one interdigital transducer (IDT) to create a travelling SAW field or two IDTs to create a standing SAW field [12, 13]. By incorporating phononic crystals into these devices, there is a huge opportunity to create new types of SAW manipulation. Examples include enhanced acoustic focusing to create SAW fields with greater force density, as well as acoustic waveguides to limit the acoustic waves to a well confined region. This paper presents the study of using microfluidic device made with a phononic crystal substrate to reflect SAWs back to the source IDT to create a standing SAW (SSAW) pattern. We focus much of our efforts on device fabrication and characterization of the phononic bandgap under varying the lattice parameters. Fluidic experiments are performed in which particles are pumped into the channel and the standing wave pattern

is observed and studied. Generation of a standing wave pattern due to the reflected energy has a powerful implication: the reflected wave maintains the phase of the transmitted wave. In other words, the SAW is reflected coherently. This is an important observation, as a fundamental necessity for well-controlled acoustic energy is coherent reflection, rather than random, disorganized scattering of acoustic waves [7]. This demonstration of reflection, paired with the novel integration of phononic crystals and microfluidics, opens up new opportunities for the future of phononic crystal devices.

## 1.2 Acoustic Microfluidics

Three decades of development have made microfluidic systems an important platform in both consumer and scientific technology. Their sub-millimeter scale allows small volumes of fluid to be processed and creates laminar flow, enabling precise control of fluids and particles [37]. This technology has given rise to a variety of functional devices, many in the fields of chemistry, biology, and medicine [13]. The flexibility of microfluidic systems enables compatibility with different types of force mechanisms to manipulate fluids and particles, including optical, magnetic, electric, and acoustic forces [15, 37].

The last decade has seen novel LOC devices created from integration of SAW technology with microfluidics [12, 13]. SAW devices generate elastic waves by transducing energy between electrical and mechanical forms. They have been integrated with microfluidics devices due to their ability to generate SAWs on the device substrate, which couple and transmit their energy to the fluid and particles inside

the channel, enabling acoustic based fluid/particle manipulations [31, 33]. There are numerous advantages of SAW base fluidics over other types of force mechanisms, especially in the realm of biological applications. SAW forces enable non-invasive manipulation such that cells exposed to acoustic fields are still viable after actuation. The contact free nature of the manipulation causes no contamination of the specimen inside the channel. Also, because IDTs are used in numerous consumer electronics, their fabrication techniques are quite developed, making the chips well-documented and very simple to make [13].

### 1.2.1 SAW Generation

The generation of acoustic waves in a SAW microfluidic device is most often realized by using a piezoelectric material as the chip substrate. Piezoelectric materials can convert mechanical stress into electrical energy and vice versa, hence the piezoelectric effect is a reversible process. Direct piezoelectric effect is the internal generation of electric charge caused by deformation of the crystal structure when undergoing mechanical stress [13]. The most common substrate for SAW based devices is lithium niobate ($LiNbO_3$).

To generate a controllable SAW that exhibits nearly planar wave fronts, an electrode geometry called an interdigital transducer (IDT) is used. [33] An IDT is a comb-shaped metallic device made of two electrodes that consist of interlocked fingers. These electrodes are used to deliver electrical energy to the substrate and when stimulated with an AC signal, the IDT causes alternating deformation of the

piezoelectric substrate, generating SAWs that propagate away from the IDT. Most of its energy is confined to the surface of the substrate within one SAW wavelength λ. This phenomenon is shown in Figure 1.1.

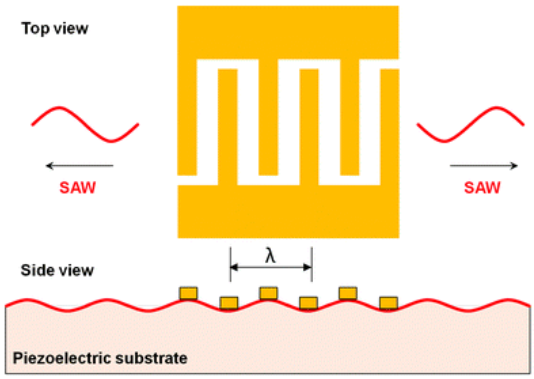


**Figure 1.1**: Generation of SAW waves using a single IDT. SAWs of wavelength λ propagate away from the IDT in both directions. They are generated due to periodic deformation of the LiNbO3 substrate [13].

There are a variety of different IDT geometries which offer properties such as higher bandwidth, higher density of acoustic power, or unidirectional SAW propagation. The bidirectional IDT, which is shown above, is most common configuration and the one we will consider further. A bidirectional IDT is designed to operate at a certain resonant frequency by selecting the appropriate acoustic wavelength λ. The finger width is usually set as λ/4, and the periodicity is λ. The frequency is then given by:

$$f_o = \frac{v_o}{\lambda}$$

is anisotropic, so the SAW velocity will differ depending on the crystal wafer cut. $128^0$ Y-X cut $LiNbO_3$ is the most frequently used crystal cut in SAW based devices, due to its high coupling coefficient and fast SAW velocity [14]. However, our electropoling phononic crystal fabrication requires us to use Z cut $LiNbO_3$, as explained in Section 1.4.

### 1.2.2 SAW Microfluidics

The most common material for the fluidic channel is polydimethylsiloxane (PDMS), an organic silicon-based polymer [15]. The channels are often made by creating a mold of the channel by patterning a silicon wafer with negative-tone photoresist, and then pouring PDMS onto the channel design. The PDMS is baked and hardened, and a negative replica of the channel is formed onto the PDMS surface. After proper surface treatment of the two surfaces, the channel is bonded to a piezoelectric substrate (or a different substrate in non-acoustic systems). A full SAW fluidic chip consists of a $LiNbO_3$ substrate patterned with one or two IDTs, and a PDMS channel bonded to the substrate near the IDT(s).

There are two main mechanisms of particle manipulation inside a microfluidic channel. A $LiNbO_3$ chip with a single IDT will generate a traveling SAW (TSAW) which propagates along the substrate away from the IDT, making contact with the PDMS and the fluid in the channel [12, 31, 33]. These waves create a traveling pressure force in the channel which will affect both the particles and the fluid inside. A chip can also be patterned with an IDT pair which will generate SAWs of the same acoustic

wavelength. These SAWs will interfere with each other to create a standing SAW (SSAW) pattern [10]. Such an acoustic field will create standing pressure regions inside the fluid, resulting in pressure nodes (minimum pressure) and anti-nodes (maximum pressure). Particles will be pushed away from the anti-nodes towards the pressure nodes.

Design of microfluidic devices requires careful consideration of the device parameters to generate forces capable of moving the target objects. Oftentimes SSAW and TSAW devices are designed to use acoustic radiation forces (ARFs) to manipulate particles in the channel. These are forces that transmit their energy to particles in the fluid, as shown in Figure 1.3(a) [12]. Particles that are strongly affected by ARFs will be manipulated by the pressure forces generated by the SAWs. This force differs between particles depending on their acoustic properties, including their size, density, and compressibility, which is how these devices can be used to sort target cells from other types of cells that are not of interest. The other force that is important to consider is the acoustic streaming force (ASF), in which the acoustic energy is transmitted to the fluid resulting in microvortices inside the fluid. Particles subjected to this force may get caught inside the microvortices. Hence, it is unfeasible to cause translational movement of particles in an ASF dominated system. Additionally, the complexity of the fluidic movement in these systems makes particle manipulation challenging to control. These forces are usually of concern in TSAW devices.

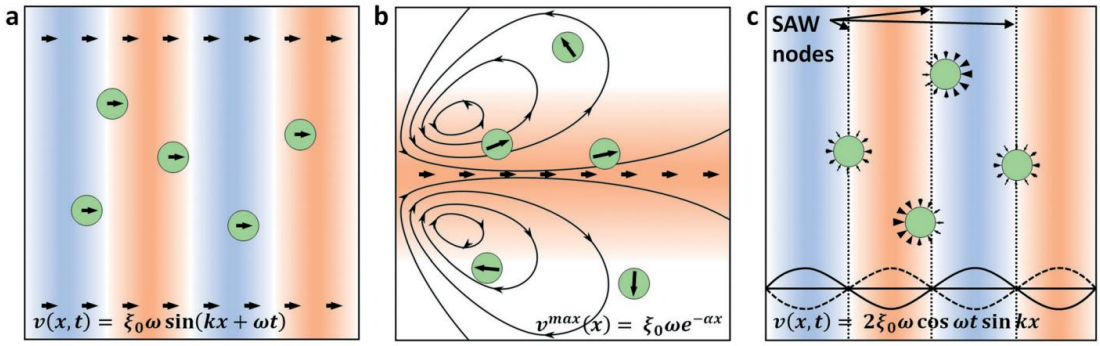


**Figure 1.2**: Three different mechanisms of microfluidic particle manipulation. A) TSAW field which consists of strong travelling SAWs that push the particles along their direction of propagation via ARFs. B) TSAW field composed of weaker traveling SAWs which generate ASF which tend to push particles in circular, disorganized trajectories, characteristic of micro-vortices. C) SSAW field which has periodic pressure nodes and antinodes. Particles tend to move towards the antinodes, where pressure is a minimum. [9]

## 1.2.3 TSAW Microfluidics

Oftentimes, TSAW devices are designed to use ARFs push target cells away from the IDT. TSAWs will also generate ASFs and tend to create microvorticies, as shown in Figure 1.3(b). These types of forces can be used for particle mixing and some forms of separation, such as separation of small particles to create particle distribution gradients. Particles exposed to a TSAW field will generally be dominated by either the ARF or ASF forces, depending on SAW wavelength and particle sizes. When ARFs dominate, particles tend to be pushed along the direction of traveling wave propagation. Dominating ASFs will tend to push particles with the fluidic motion.

Analytical calculation of the force generated by the ARFs and ASFs and further comparison is mathematically demanding. Rather, what is often done is calculation of

the Helmholtz value κ [11]. This value is a rough but useful estimation of whether a particle will be subject to dominating ARFs or ASFs.

The formula for κ is:

$$\kappa = \frac{\pi f_{TSAW} d_p}{c_f}$$

where $f_{TSAW}$ is the frequency of the TSAW, $d_p$ is the particle diameter, and $c_f$ is the acoustic speed within the fluid of the channel. For water, $c_f$ is about 1450 m/s [11]. For particles with $\kappa > 1$, the ARFs tend to be the dominating force, enabling particle deflection within the channel [9]. In general, a κ value slightly higher than 1, such as 1.1-1.2 is necessary to see a noticeable effect. When $\kappa < 1$, ARFs are weak and particles will not travel along the direction of TSAW propagation. κ is a size dependent parameter, and differing sized particles exposed to the same system will likely undergo different force magnitudes and have different deflection lengths. However, it does not take into account acoustic properties of the particles, such as shape or density. For such experiments, actual forces will need to be calculated. The κ value is also frequency dependent, so higher frequency SAWs will deflect a larger range of particles. This is an important design parameter, such that IDTs are designed in order to cause the κ will be appropriate for the particle of interest.

### 1.2.4 SSAW Microfluidics

Because of the periodic force field of the standing wave pattern, mathematically describing particle forces under a SSAW field is much more straight forward than a

TSAW system. ARFs are again the important force to consider for SSAW particle manipulation. Particles are attracted to the nodes or anti-nodes of the pressure within the fluid. Particles moving under the ARFs also experience a viscous force that dampens the radiative effect. The two forces are described with the following equations [31].

$$F_r = -\left(\frac{\pi p_o^2 V_p \beta_m}{2\lambda}\right)\phi(\beta,\rho)\sin(2\mathrm{kx})$$

$$\phi(\beta,\rho) = \frac{5\rho_p - 2\rho_m}{2\rho_p + \rho_m} - \frac{\beta_p}{\beta_m}$$

$$F_v = -6\pi\eta r v$$

For the radiation force $F_r$, $p_0, \lambda, k, V_p, \beta_p, \beta_m, \rho_p, \rho_m$ correspond to the acoustic pressure, acoustic wavelength, wavenumber, particle volume, particle compressibility, medium compressibility, particle density, medium density, respectively. The function $\phi$ is the acoustic contrast factor, which describes whether the particles will be attracted to the pressure nodes ($\phi > 0$) or anti-nodes ($\phi < 0$). The viscous force is dependent on $\eta, r,$ and $v$, which are the medium viscosity, particle radius, and particle velocity. As we can see $F_r \propto r^3$ while $F_v \propto r$ [13]. This causes ARFs to become large very quickly as particle size increases. This difference in force magnitude creates a strong cell separation mechanism, as larger cells will be pushed towards node lines much quicker than small cells.

## 1.3 Phononic Crystals

Phononic crystals (PnCs) are artificial materials that are designed to control the propagation of phonons through the material [25]. They are composed of two materials that differ in their acoustic impedances, generally in the form of a solid or fluid matrix with a periodic repetition of hole or pillar inclusions. A major step in the process of developing phononic crystal technology is creation of a phononic bandgap, a region of acoustic wave frequencies that are unable to propagate through the crystal structure [23]. A bandgap is a fundamental material property in fields of electronics and photonics. An electronic bandgap prevents electrons with certain energy levels to exist in a semiconductor, and a photonic bandgap prevents a range of photonic frequencies to exist in a photonic material.

### 1.3.1 Phononic Crystal Background

The field of phononic crystals has been expanding since the early 21$^{st}$ century, outputting a variety of different fabrication techniques and phononic functionality. Novel geometries have created phononic crystals that manipulate acoustic waves in a variety of mechanisms [25]. More impressive is the frequency range of phononic crystal devices and the functionality that arises [17]. Early phononic structures aimed to manipulate phonons in the sonic and ultrasonic frequency ranges, and are very large compared to lab-on-a-chip devices. While simple to create, phononic structures on this scale laid out fundamental steps for the field of phononic crystals. Ultrasound phononic

crystals manipulate sub-millimeter acoustic waves and are small enough to go on a chip. This acoustic frequency range is the same that enable current acoustic LOC technology such as SAW-based chips.

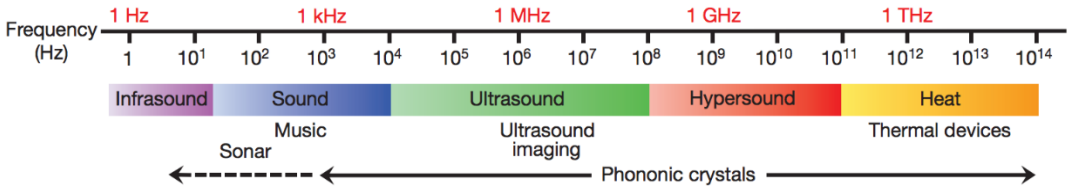


**Figure 1.3**: Spectrum of acoustic frequencies. The low end of the spectra includes audible soundwaves as well as sonar. Phononic crystal are generally fabricated above the high kilohertz region. Megahertz devices are useful due to their compatibility with SAW technology. Hypersonic is additionally an explored area with applications in phononic/photonic devices. In the terahertz, we tend to see devices used for heat transfer manipulation. [25]

The hypersonic frequency regions has enabled some very interesting devices [17]. Hypersonic crystals requires phononic structures that operate on phonons with the same wavelengths as those of light wavelengths, which has opened the opportunity to create materials that create interactions between phonons and photons, including opto-mechanical oscillators[14]. Thermal devices operate on phonons with frequencies in the terahertz range, and are very challenging to fabricate due to their sub-micron structures. However, there has been successful fabrication of phononic structures with features that are small enough to interact with thermal phonons to significantly reduce their propagation speed, which have been used to tune the thermal conductivity of a material. [18, 38] These have been of great interest due to the need to dissipate heat in

order to continue to improve silicon-based electronics performance, as well as thermo-electric devices for new means of energy harvesting.

### 1.3.2 Surface Acoustic Wave Phononics

While many phononic crystal devices are used to manipulate phonons that propagate through the bulk of a material, they can also be used to manipulate those that propagate across a material's surface.[14, 15, 18, 38] This creates opportunity to integrate phononic crystals with SAW devices to further expand their functionalities. SAW devices have been heavily studied and utilized for the last 60 years, which has given them a simple design and fabrication process. and allow for precise control of propagation of SAW waves on a material. SAW waves are easy to stimulate using an IDT, which can be easily designed for specific applications. They are therefore very useful in the field of phononic crystal research.

### 1.3.3 Mechanisms of Creating Phononic Bandgaps

There are two main mechanisms for creating SAW bandgaps. The first is Bragg scattering, which is caused by creating a periodic alternating of the elasticity, density, or piezoelectricity of the substrate material [17, 23, 30, 41]. This alternation of the material properties creates interfaces inside of the crystal. When acoustic waves hit these interfaces, some energy is transmitted and some is reflected. If transmitted waves interfere with each other constructively, the majority of the energy is transmitted through the crystal which allows the SAW to propagate across. However, if the

transmitted waves destructively interfere with each other, the energy is reflected back and acoustic waves cannot propagate. These types of crystal are often made by etching finite-depth holes into a substrate to create air inclusions, which differ from the substrate in density and elasticity. The holes can be filled with another material, but this is less common. This Bragg scattering effect is analogous to the mechanism that causes photonic band gaps, which appears in materials that have a periodically reversing refractive index.

The other common mechanism is local resonance, which occurs at frequencies below the Bragg limit. [1, 2, 3, 21] This is often achieved by depositing additional features on the surface of the crystal such as pillar which are designed to resonate at a specific frequency, similar to a mechanical mass-spring system. SAWs that operate at frequencies near the resonance of the pillars will couple and transmit their energy to the pillars, which will prevent further transmission of the waves. SAWs that do not stimulate the pillars will be negligibly attenuated.

While far less studied, there is a third mechanism for creating phononic bandgaps that poses many advantages to the previously mentioned methods. This bandgap is a result of lithium niobate's piezoelectric properties, which enables the coupling of the acoustic wave vibrations and the electromagnetic waves excited by electrodes on the $LiNbO_3$ [19, 20]. This coupling results in what is known as a phonon-polariton. [39, 40] However, a pure $LiNbO_3$ substrate will not exhibit this kind of coupling. Instead, a periodic reversal of the piezoelectric domains is required to

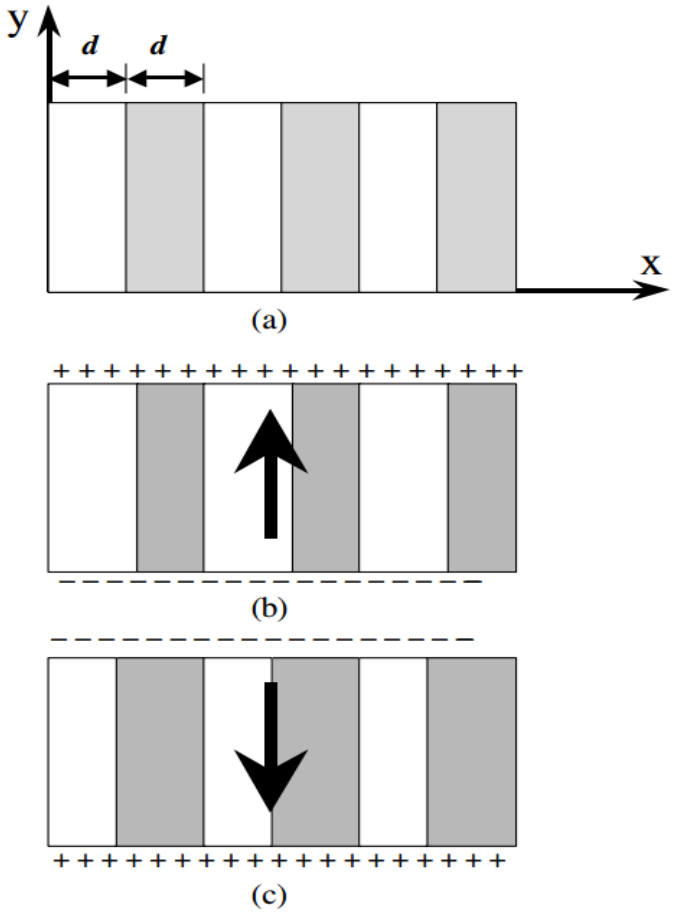


**Figure 1.4**: Interaction between periodically poled LiNbO3 (PPLN) and electromagnetic radiation. (a) The PPLN in its unbombarded state, the gray regions depicting +z domains and white depicting -z. The z axis is normal to the paper. (b) The PPLN under EM field with +y polarization, causing the -z regions to contract and the +z to expand. (c) the PPLN under –y polarized EM field, with gray region expanding and white regions contracting. This behavior generates a coupling of the EM with the SAW which results in a bandgap formation. [43]

generate such an effect. This type of structure is called a piezoelectric superlattice (PSL), meaning an artificial lattice with a lattice constant much larger than that of an atomic structure. PSL lattice constants are generally on the order of 1-100 μm in size, and are made by reversing the direction of the piezoelectric domain of a homogenous substrate, often by a method of electropoling. [26] The periodic nature of the PSL

offers unique properties that differ greatly from its homogenous counterpart, including the ability to couple acoustic vibrations to electromagnetic waves.

To understand how this seemingly unintuitive topic works, let us consider the following system. We have a $LiNbO_3$ with periodic inversion of its ferroelectric domains along the x-axis. The domains are modulated to face either the +z or –z direction (Fig 1.5(a)). When undergoing no external electric field, both the negative and positive domains are of equal size *d*. Now consider a +y polarized EM wave propagating across the crystal in +x direction. The wavelength of the EM wave is much larger than that of the crystal lattice constant 2*d*, so we can consider the cases where the crystal is undergoing a nearly constant electric field along its x axis. As shown in previous studies, the positive and negative piezoelectric domains will undergo opposite mechanical stresses when exposed to the electric field [43, 44]. In Figure 1.5(b), the electric field causes the positive charges to appear on +y side of the crystal in both the positive and negative piezoelectric domains. In order for the superlattice to maintain electrical homogeneity, the negative domains must contract while the positive domains expand. The large arrow shows the electric polarization across the PSL. The opposite case is shown in Figure 1.5(c). This compression and decompression of the different piezoelectric domains results in a longitudinal vibrations that propagates in the x-direction of the lattice. This superlattice vibration is both excited by and couples to the y-polarized EM wave. As we can see, the interaction between the electromagnetic wave and acoustic vibration is a result of the piezoelectric effect of the substrate.

The equations of motion of the EM and acoustic waves of this system are described using Newton's and Maxwell's laws:

$$T_1 = C_{11}^E S_1 + e_{22}(x) E_2$$

$$P_2 = -e_{22}(x) S_1 - \varepsilon_0 (\varepsilon_{11}^S - 1) E_2$$

In this system, $T_1, S_1, E_2,$ and $P_2$ are the stress, strain, electric field (y direction), and electric polarization (y direction), while $C_{11}^E$, $\varepsilon_0$, and $e_{22}(x)$ are the elastic, dielectric, and piezoelectric constants, respectively, where $e_{22}(x)$ is a function of x, reversing direction periodically to represent the periodic modulation of the piezoelectric domains [43]. The second equation implies that the longitudinal wave $S_1$ induces the polarization $P_2$, which produces the EM wave that couples to the original EM wave. While mathematically intensive, these equations can be used to derive various relationships between EM and acoustic waves in the PSL. These relationships are beyond the scope of this thesis, but can be seen in references 42 and 43.

## 1.4 Fabrication of Phononic Crystals

The growth of phononic crystal field has produced new fabrication technique to make such crystals. Phononic crystals that operate using Bragg scattering often are formed by etching holes in the crystal substrate. Such etching often requires expensive machineries to perform procedures such as deep ion etching or for focused electron beam etching [5]. Such machines are useful if already available, but very expensive.

Locally resonant phononic crystals require pillar arrays to be fabrication on the crystal. They are often made of metal, and deposited using electroplating techniques [21]. Electroplating can be a cheaper fabrication, but because of the small size of the extruding pillars, they can be easy to break. Additionally, the uneven surface topology can make these incompatible with microfluidic technology [39].

Phonon-polariton bandgaps, which are fabricated with an electropoling method, require a cheap setup and have a completely homogenous surface topology, making crystals that are not just microfluidic system compatible, but also compatible with adding additional layers and functionalization [39]. The technique is done by applying a high voltage across a crystal wafer to switch the domain direction. Photolithography is used to pattern the crystal to select the regions of the crystal to switch the domains. This modulates the periodicity of the piezo-electric domains but keeps all other properties homogenous Domain reversal of $LiNbO_3$ via electropoling has been explored for over 25 years for photonic applications, as the poled regions also differ in refractive index which has enabled the creation of non-linear optical devices [29]. Compared to traditional PnC fabrication methods including reactive ion etching and focused ion beam lithography, such a setup can be built for far less than the purchase of an expensive piece of cleanroom equipment.

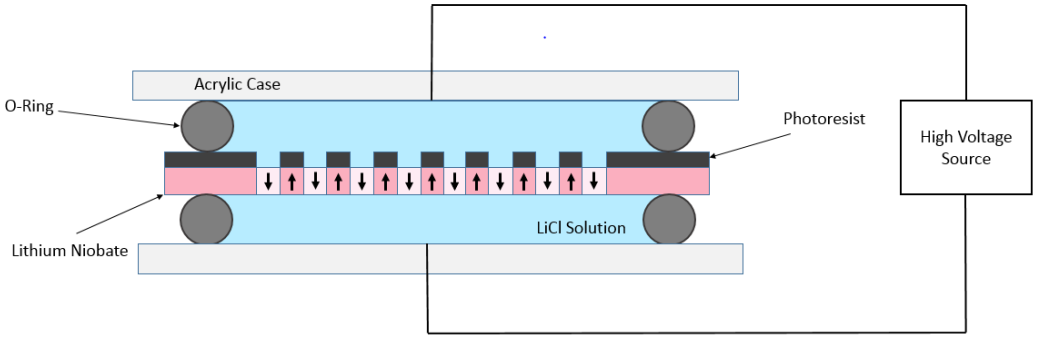


**Figure 1.5** - A periodically poled LiNbO3 crystal, undergoing domain reversal under strong electric field generated by HV source. Photoresist is used to cover areas so they do not become poled, while uncovered areas switch domain direction. 10M LiCl is used to make electrical contact with the wafer.

## 1.4.1 Properties of $LiNbO_3$

Ferroelectricity is the property that lithium niobate exhibits to allow it to be periodically poled. This gives the material a permanent spontaneous polarization. The direction of the polarized domains can be reversed by applying an electric field across the sample to shift the position of the charged ions. For $LiNbO_3$, the electric field must exceed the coercive field voltage of 21 kV/mm. [29]

Studying the crystal structure of $LiNbO_3$ offers further understanding of this concept. $LiNbO_3$ is composed of the ions $Li^{+}$, $Nb^{+5}$, and $O^{-2}$ [35]. While these charges are balanced in a unit cell, a spontaneous polarization is formed by internal electric dipole moments resulting from the positions of the charged ions[8, 36]. The crystal structure of $LiNbO_3$ is composed of planes of $O^{-2}$, and the area between planes are filled

with either $Nb^{5+}$, $Li^{+}$, or an ion vacancy. This structure alternates between vacancy, Nb, Li, vacancy, Nb, Li, etc. These oxygen ion planes are defined by 3 oxygen ions, which actually create an octahedral structure with the adjacent plane in c direction (analogous to the z direction). Figure 1.7 is provided for better illustration.

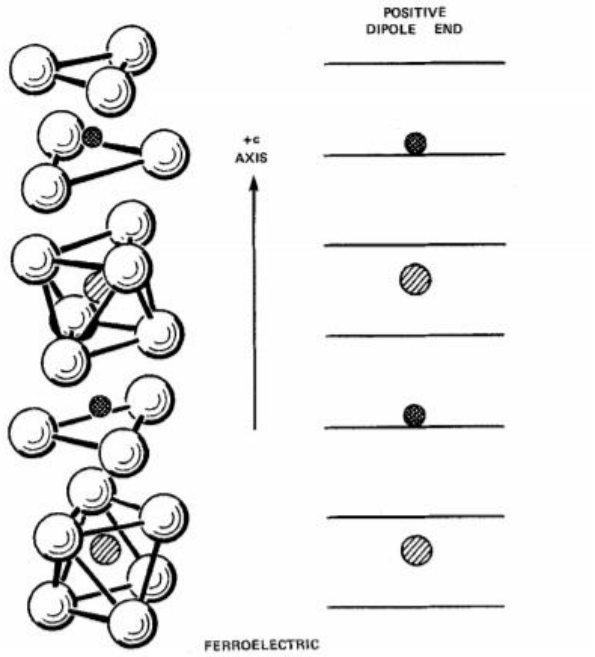


**Figure 1.6**: LiNbO3 that is polarized in the +z (+c) direction. Notice that the positively charged $Nb^{5+}$ and $Li^{+}$ ions are shifted up relative to the negatively charged $O^{-2}$ ions, generating a positive polarization in the +z direction and negative polarity in the -z direction [36].

In this state crystal exhibits spontaneous polarization. Its polarization is created by a slight shift of the positively charged $Nb^{5+}$ and $Li^{+}$ in the C direction, such that they are no longer in plane with the oxygen atoms. Figure 1.7 shows the Li and Nb ions located slightly further in the +z (+c) direction than their paraelectric positions, creating a spontaneous polarization in the +z direction

### 1.4.2 Electropoling of $LiNbO_3$

The coercive field voltage is the field that must be applied to a material in order to reverse the piezoelectric domains of the crystal [26, 27]. For $LiNbO_3$, this value is about 21 kV/mm. For our 500 μm wafers, the coercive field should be about 10.5 kV. The dielectric nature of the crystal generally prevents current to flow through. However, when the coercive field voltage is applied to the crystal, current begins to flow as the domains are reversed. The domain reversal brings rise to opposing forces inside of the crystal causes the voltage clamp at the coercive field voltage [29]. In order for successful poling, the current must apply enough charge to fully reverse the domain directions. This charge is given by

$$Q = 2PsA$$

where *A* is the poled area and *Ps* is the spontaneous polarization, which is in terms of Charge/Area. In order to completely flip the crystal polarization, the magnitude of the polarization vector ***P*** must be flipped from $P_s$ to -*Ps*, which requires a magnitude change of 2*Ps*.

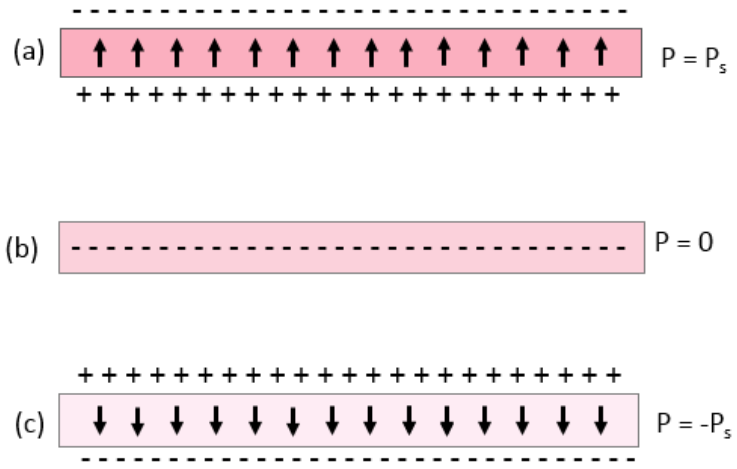


**Figure 1.7**: (a) Z-cut LiNbO3 when polarization in +z axis is maintained at Ps. (b) Application of Q = PA causes domains to be neutralized, creating no polarization. (c) application of Q = 2PA causes domains to completely reverse, creating a polarization of –Ps, with same magnitude as original but opposite in direction.

The amount of charge applied to the sample is calculated by $Q = \int i\, dt$, and therefore can be found by integrating the current data from the beginning of the poling process to the end. The spontaneous polarization can then be calculated as $Ps = \frac{\int i\, dt}{2A}$. When the voltage clamps during poling, the voltage and current are fairly static. Once enough charge has been applied to the sample and the domain reversal is nearing completion, the current begins to fall. Once the poling has completely finished, the current stops flowing through the sample and the voltage across raises to the fully applied voltage. [29]

# Chapter 2: Methods

## 2.1 Device Fabrication

### 2.1.1 Electropoling Setup

An electropoling setup was designed and built in order to perform this fabrication. The setup aims to reverse the piezoelectric domains by applying a voltage of 10.5 kV to the sample while controlling the amount of current that goes through the crystal. The poling rate is proportional to the current through the crystal, so this parameter is of key importance. The setup is designed to monitor both the voltage across the sample and the current through it to observe the poling process. The hardware design was adapted from electropoling setups described in previous studies and was adjusted to fit our systems [26, 27, 29, 35]. The circuit is shown Figure 2.1.

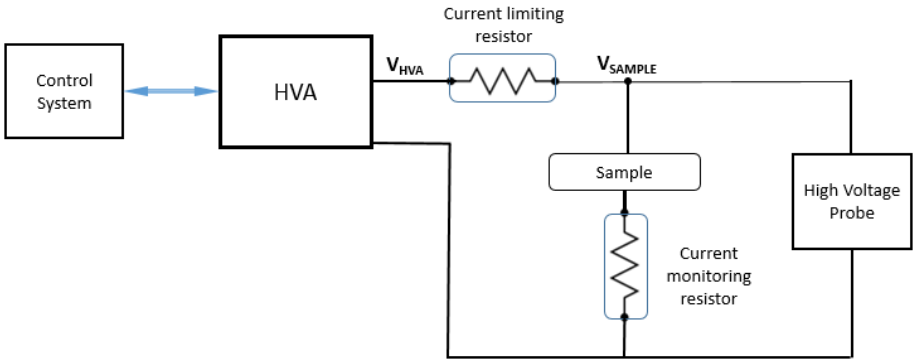


**Figure 2.1**: Block diagram of the electropoling setup. The control system takes in user input, controls the HVA, and datalogs poling current and voltage data. The Ultravolt HVA generates a ~12kV signal to the system to pole the sample. The current limiting resistor (50MOhms) controls the amount of current and therefore the poling rate of sample. The high probe down-converts (10GOhm) the high voltage signal so it can be logged by the control system, and the current monitoring resistor (50KOhms) generates a small voltage proportional to the poling current that can also be monitored.

The control system implemented with a National Instruments DAQ (NI-USB 6002) which controls the high voltage amplifier (HVA) using programmable I/O and provides data acquisition for logging voltage and current data. The DAQ is controlled using a custom LabVIEW program, which allows a user to control the amount of poling voltage and the duration of the poling voltage.

The DAQ generates the poling signal, which is amplified by a factor of 2000 using the HVA. The output is applied to node $V_{HVA}$. The sample is placed in series with a 50 MΩ current limiting resistor $R_{LIMIT}$, which functions to control the amount of current that goes through the sample during the poling process. When $V_{SAMPLE}$ is below the coercive voltage, the sample is non-conductive and acts as an open circuit. Once $V_{SAMPLE}$ reaches and surpasses the coercive voltage, the node clamps 10.5 KV. Therefore $V_{SAMPLE}$ is at a set voltage, and the current that goes through the sample is given by:

$$i_{poling} = \frac{V_{HVA} - V_{sample}}{R_{limit}} - \frac{Vsample}{RHVP}$$

However, because $R_{HVA}$ is three orders of magnitude greater than $R_{LIMIT}$, we can accurately approximate the poling current to:

$$i_{poling} = \frac{V_{HVA} - V_{sample}}{R_{limit}}$$

Because the $LiNbO_3$ sample clamps at the coercive voltage, the current in the system can be controlled by changing output of the HVA or changing the value of the current limiting resistor. Higher voltage and lower resistance will create larger currents, which

will reverse the domains quicker. Conversely, a lower voltage and high resistance will generate a lower, more controlled current.

The voltage is monitored by a high voltage probe, which down-converts the high voltage signal by a factor of 2000 so it can be safely read with the DAQ. The current is monitored by a series resistor of 50kΩ. Because of its small resistance compared to the $LiNbO_3$ sample and current limiting resistor, it adds negligible resistance to the current path. However, the voltage across it does go up to a value between 0-5V during the poling process, making it easy to monitor with the DAQ. Between the current monitor resistor and the high voltage probe, we are fully enabled to monitor the voltage and current data throughout the poling process. The full setup and poling chamber can be seen in Figure 2.2.

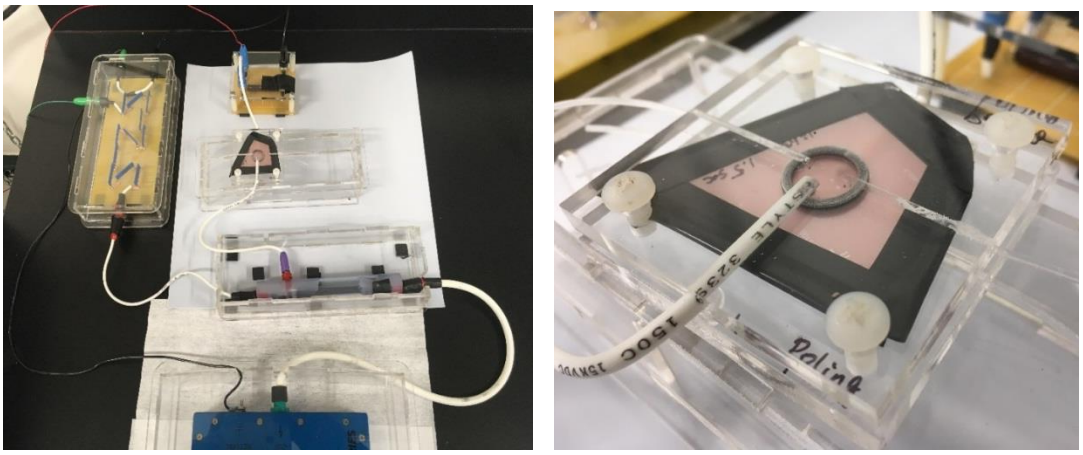

**Figure 2.2**: (a) The electropoling setup with a patterned LiNbO3 sample. (b) The electropoling chamber with sample. The chamber includes two layers of acrylic which has drilled holes for tubing to insert liquid and high voltage wires. O-rings are used to sandwich sample inside chamber.

Care was taken to ensure no injury to users or damage to equipment would occur. The current limiting resistor is placed in a PVC pipe filled with silicone rubber for complete isolation and safety, and the high voltage probe was entirely in a thick acrylic case for electrical isolation from other components and people in vicinity. Heavily insulated wire with high voltage safety ratings were used for high voltage connections, and junctions were wrapped in high voltage electrical tape when appropriate. By designing the setup with safety as a fundamental design component, no issues were encountered.

### 2.1.2 Phononic Crystal Fabrication

Fabrication of the phononic crystals requires three photolithographic processes on a single wafer. The three processes were done to add alignment markers to the wafer, create a phononic crystal pattern that would undergo electropoling, and to add IDTs to the devices, respectively. This process is depicted in Figure 2.3.

Z-Y cut $LiNbO_3$ wafers were used to fabricate our devices. This cut is used due to its compatibility with our electropoling method. Metallic alignment markers were patterned onto the $LiNbO_3$ wafer to ensure proper alignment of the IDTs with respect to the phononic crystal pattern. Incorrect placement of these structures will result in poor interaction between the SAW and phononic crystal pattern. The process began by spin-coating the wafer with S1818 photoresist to create a 3 μm layer. UV photolithography was used to pattern the photoresist with the alignment markers. The wafer was developed, hard baked, and treated with $O_2$ plasma for 5 minutes to get rid of any excess photoresist. Electron-beam evaporation was then performed to deposit a

5 nm layer of Ti followed by 50 nm of Au on the wafer. A lift-off procedure was performed by sonicating the wafer in acetone to get rid of excess metal and photoresist, leaving only the alignment markers on the $LiNbO_3$ wafer.

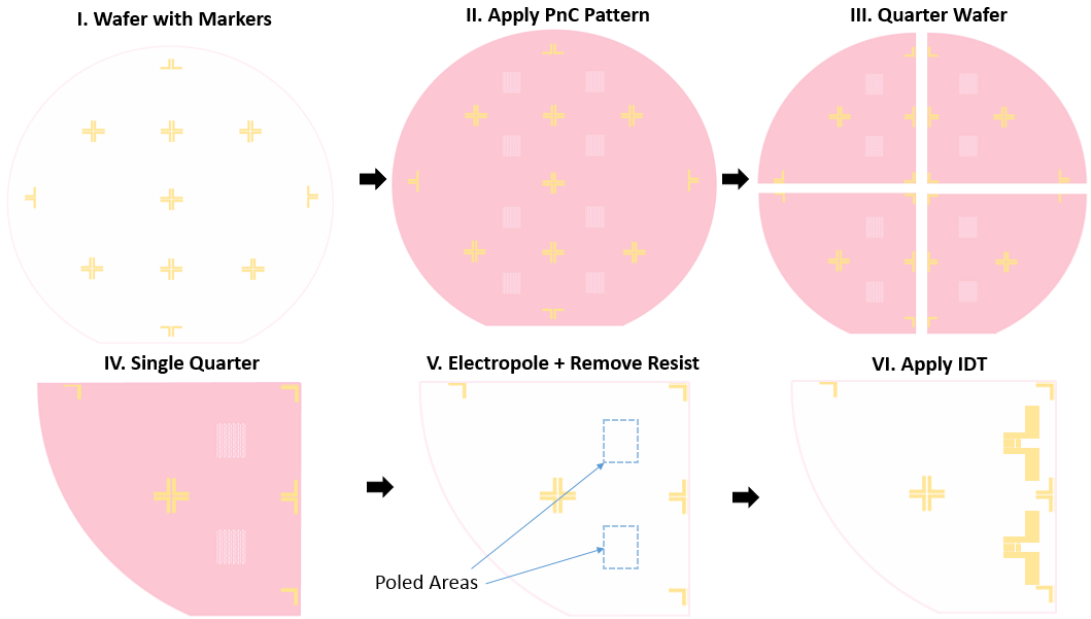


**Figure 2.3** Fabrication procedure of PnC devices. (i) Pattern wafer with alignment markers via photolithography and gold evaporation. (ii) Apply PnC pattern using S1818 photoresist. (c) Cleave wafer into four quarters, such that each substrate has two devices. This is due to the fact that z-cut LiNbO3 is challenging to cleave into smaller components. (d) Single quarter of wafer resulting from cleaving. (e) Each PnC region on substrate is electropoled. Photoresist is then removed, leaving clean wafer. (f) IDTs are applied to wafer quarter.

Next the phononic crystal pattern is applied and electropoling is performed. S1818 photolithography is performed using the same process as the alignment markers. The photomask is designed to place eight devices on a single wafer, and the alignment markers are used for proper position of the PnC region. Development and hard baking are again completed. The photoresist is the hard and durable so the phononic crystal pattern won't be deformed. The wafer is then quartered such that two phononic crystals are on a single device.

The substrates then undergo electropoling to reverse the domains of the regions that are not patterned with photoresist. The chamber is designed to fit a substrate that is a quarter of the full $LiNbO_3$ wafer. The PnC region is placed inside the O-rings of the chamber, and lithium chloride solution is used as a liquid electrolyte to make electrical contact with each side of the wafer. High voltage is applied to the crystal, creating functional a PnC in under 5 seconds. After poling is completed, the wafer is rinsed in acetone to get rid of the photoresist. The wafer looks completely cleaned after this process, with only the alignment markers remaining.

The IDTs are then applied to each substrate. This process is done with S1818 photolithography, the alignment markers used to place the IDT in the correct location with respect to the phononic crystal. The photolithography is completed and electron-beam evaporation is used to apply 5 nm of Ti and 120 nm of Au to the wafer, followed by a lift-off procedure.

## 2.1.3 Microfluidic Channel Fabrication

The microfluidic device was made with a standard soft photolithography procedure. SU8-2050 negative photoresist was spin-coated on a Si wafer, and the channel design was lithographically patterned. The resist was developed and hard baked. PDMS was prepared with a 10:1 base to elastomer ratio and poured on the patterned wafer. The wafer was cured at $60^0$ C for two hours, and the PDMS was removed and cut to form individual channels. The devices were completed by bonding the channel to the phononic crystal substrate by treating both components with UV ozone for 15 minutes. The channel is aligned to the IDT and crystal and then place overnight in a $60^0$ C oven to complete the bonding. The final device is shown in Figure 2.4.

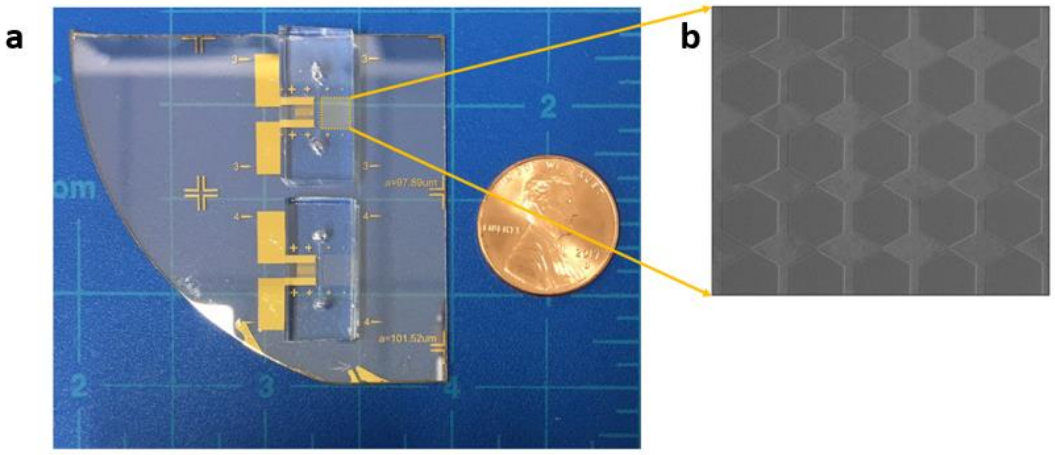


**Figure 2.4**: (a) Fully fabricated microfluidic PnC device with coin as reference. (b) Electropoled region of hexagonal array pattern after HF etching treatment, which helps reveal reversed domains.

## 2.2 Bandgap Design and Simulation

Our initial studies were performed on 1D PnC devices which have a very simple geometry. The bandgap location of these devices can be easily adjusted changing the periodicity of the design. This geometry offered a simple platform to develop our experimental methods, which included initial studies on electropoling fabrication, bandgap characterization, and microfluidic experiments. After laying out the foundation for fabricating and studying these devices, we then expanded our design to the 2D PnC device. In order to design the PnC structures, COMSOL allows us to simulate the phononic bandgap while varying the lattice parameters. However, due to fabrication variations and imperfections in the simulation parameters, these simulations are useful for finding an approximate bandgap region, and then use experimentation to identify the bandgap location and adjust the design as needed.

### 2.2.1 One Dimensional PnC Device

A one-dimensional PnC device was designed, which rejects phonons in only the x-direction. For this design the phononic crystal region is composed of bands of periodically poled $LiNbO_3$, as shown in Figure 2.5 (a). The finite element method (FEM) was used to calculate the bandgap for this phononic lattice structure by solving the eigenvalues for the equations of motion that govern the propagation of EM and acoustic waves:

$$\boldsymbol{T} = C^E : (\nabla_s \cdot \boldsymbol{u}) - \boldsymbol{e}^T(x) \cdot \boldsymbol{E}; (a)$$

$$\boldsymbol{D} = \varepsilon^S \cdot \boldsymbol{E} + \mathrm{e}(x) : (\nabla_s \cdot \boldsymbol{u}); (\mathrm{b})$$

$$\nabla^2 \boldsymbol{E} = \mu_0 \, \partial_t^2 \boldsymbol{D}; (c)$$

$$\nabla \cdot \boldsymbol{T} = \rho \, \partial_t^2 \boldsymbol{u}. (d)$$

Where $T$, $\mu$, $E$, $D$, $C^E$, $\rho$, and $\varepsilon^s$ are stress, elastic field, electric field, and electrical displacement, stiffness, density, and dielectric constants, respectively. The piezoelectric coefficients $e(x)$ equals +1 for non-inverted domains and -1 for inverted domains to reflect the periodically reversed structure of the device. The thickness of the domains was set to $a/2$, one half the periodicity. The phononic bandstructure of this system which is depicted in Figure 2.5 (a) was numerically simulated. By adjusting the periodicity $a$ of the structure the bandgap can be adjusted to place in a desirable region. Our studies were done on a PnC with a periodicity of 97.89 μm. The simulated bandgap is shown in Figure 2.5 (b).

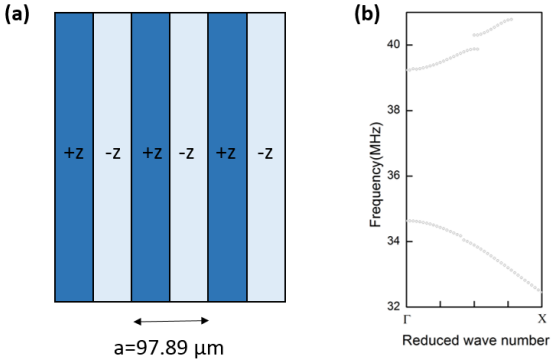


**Figure 2.5:** (a) One dimensional PnC device with a lattice constant of 97.89 μm, which consists of one period of domain reversal. (b) simulated bandgap of 1D device with lattice constant of 97.89 μm, resulting in a large bandgap near 37 MHz and a smaller bandgap near 40 MHz.

As we can see, a lattice constant of 97.89 μm generates a large bandgap centered at 37 MHz, with a bandwidth of nearly 4 MHz. In addition, there is a narrow bandgap at 40 MHz with a 0.5 MHz bandwidth. These results serve as a reference for our experimental results. It must be remembered that this bandgap is simulated for perfectly fabricated devices, and variations in fabrication can lead to deviations from the simulated results.

### 2.2.2 Two Dimensional PnC Device

The two-dimensional PnC expands the SAW rejection to both the x and the y direction. The design of this crystal is a honeycomb lattice pattern with hexagonal inclusions, as shown in Figure 2.6(a). Our FEM simulation again finds the eigenvalues of the equation set above, which is both dependent on the PnC lattice period and hexagonal side length. A bandgap simulation of a 2D PnC with a periodicity of 100 μm and a hexagonal sidelength of 20 μm os shown in Figure 2.6 (c). It has a resulting bandgap centered at 44 MHz, offering approximate dimensions to the design we will use in our studies. However, the final design for the 2D device is decided after studying the 1D results and deciding a bandgap region of interest.

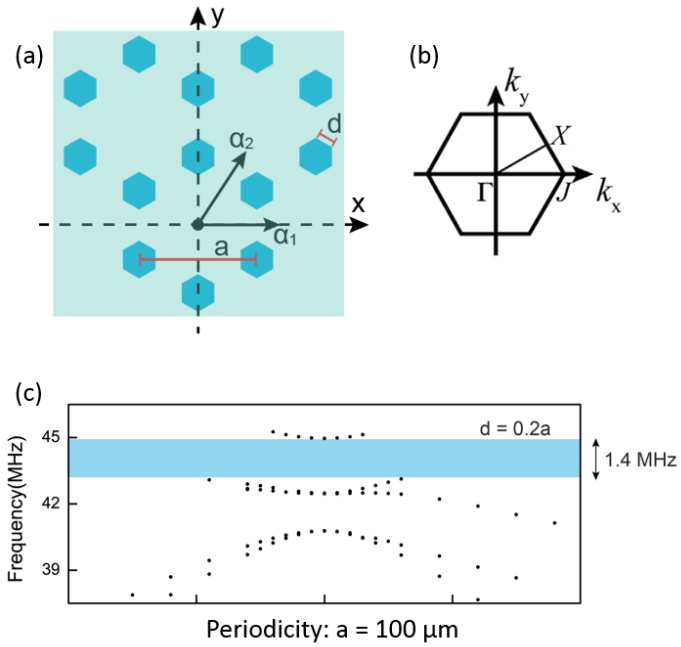


**Figure 2.6:** (a) 2D PnC pattern consisting of a honeycomb lattice with lattice constant a and hexagon sidelength d. (b) Brillouin zone for honeycomb lattice, with irreducible brillouin zone ΓXJ. The ΓX direction in k-space maps to the y direction in real space, while the ΓJ direction maps to the x direction in real space. (c) Simulation results for a PnC with a = 100 μm and d = 20 μm, exhibiting a bandgap centered at 44.3 MHz with a 1.4MHz bandgap.

## 2.3 Characterization of PnC Bandgap

In order to experimentally observe the bandgap in order to compare it to the simulated bandgap, we use wideband IDTs to identify SAW frequency rejected by the PnC device. Slanted IDTs are designed to have a longer wavelength on one end of the IDT, and a smaller wavelength at the other, as shown in Figure 2.6(a). This geometry enables the IDTs to be excited with a wide band of frequencies [24]. The output of the wideband IDT is shown in Figure 2.6(b). By fabricating a PnC region between two

SIDTs, we can identify dips in the wideband signal that indicate frequency bands that are rejected by the PnC. This enables us to compare the experimental behavior of our PnC devices to their simulated behavior, thus providing us insight which allows us to connect our fabrication, experimental results, and simulations together.

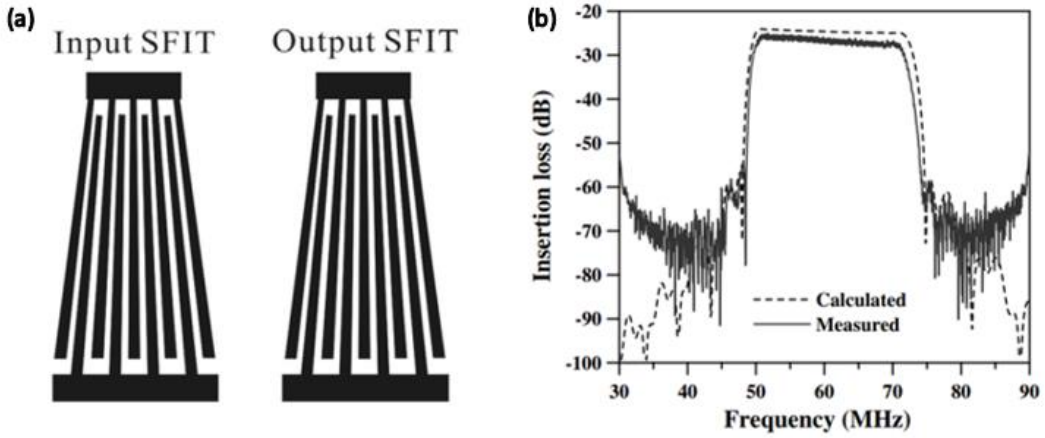


**Figure 2.7**: (a) Slanted IDT design with a geometry that contains a wavelength gradient, such that the top side generates high frequency SAWs and the bottom side generates low frequency SAWs. (b) Wideband signal generated by a SIDT. [24]

## 2.4 Microfluidic Experimental Setup

Microfluidic experiments were performed on microfluidic PnC chips to observe the interaction between the SAWs and PnC region. Samples were prepared with 2.2 μm green fluorescent polystyrene beads in a 0.1% bovine serum albumin (BSA) solution for a bead concentration of $10^5$/mL . The channel consisted of a single inlet and outlet, through which fluid was pumped through at 0.46 μL/min using a motorized syringe pump. An RF generator (Agilent) was used to excited the IDTs with a

frequency near 43 MHz, the IDT resonance. The RF generator output a 4V signal which was amplified to using a Mini-Circuits RF amplifier to achieve a signal of 8V. A digital network analyzer was used to measure the reflection and transmission data of the IDT(s). During experimentation, the device was placed under a fluorescent light source and observed with a TiE 2000 microscope. The beads could then be observed to study the SAW field generated by the phononic bandgap of the PnC device.

# Chapter 3: Results

## 3.1 Electropoling Evaluation

Evaluation of the electropoling setup was done with by applying high voltage to a blank $LiNbO_3$ crystal and recording the poling voltage and current. This was done in two trials, the first applying an output voltage of 12 kV and the second applying 11.5 kV. Poling could only be successfully carried out by applying voltage to the +z crystal direction, which caused the +z domains to switch to the –z direction. If the crystal was placed incorrectly, poling would not occur. The current data was integrated to calculate the spontaneous polarization constant. Results are shown in Figure 3.1:

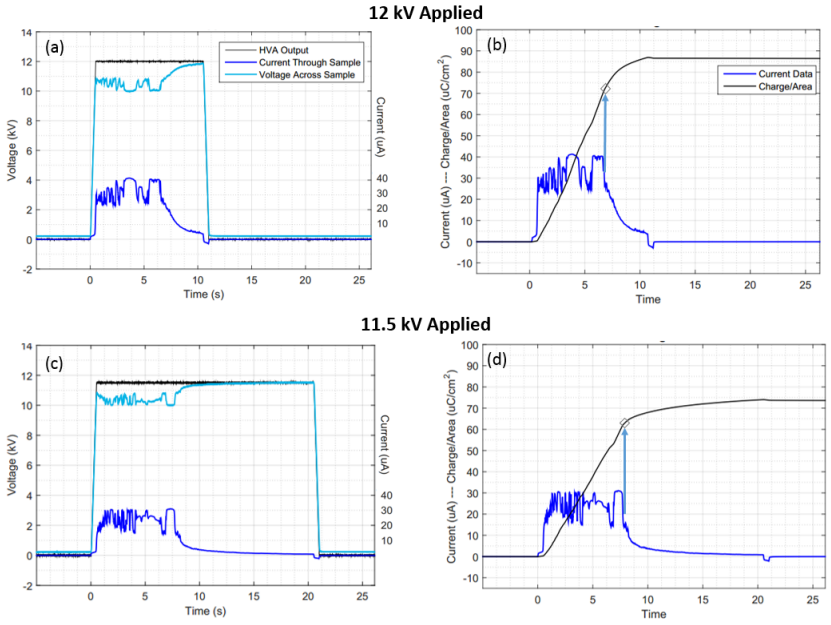


**Figure 3.1**: (a) Electropoling current and voltage data for sample poled at 12 kV. (b) Data for sample poled at 11.5 kV. (c) Current data (blue) and charge/area data (black) for 12 kV pulse. Spontaneous polarization is charge/area value found when poling current diminishes. (d) Current and charge/area data for 11.5 kV pulse.

The voltage across the substrate dropped from the $V_{HVA}$ to a lower voltage of about 10 to 10.5 kV in all trials. This indicates the voltage across the sample adjusted to the coercive voltage of $LiNbO_3$, confirming successful poling. The Figure 3.1 (a) and (c) shows the voltage dropping as poling process begins, and then rising back to $V_{HVA}$ once the $LiNbO_3$ domains are fully reversed. Note that the current lasts 6.3 seconds for the 12 kV trial and 7.21 seconds for the 11.5 kV trial. The current is also higher for the 12 kV trial as well, ranging between 25-40 μA, while the 11.5 kV trial hovers between 17-30 μA, demonstrating how the poling process can be controlled by varying the HVA voltage.

The resulting current data is then integrated using Matlab to generate the charge data. This charge data is divided by the poling area of 1.418 $cm^2$ to put the data in units of charge/area, the same units as the spontaneous polarization. The spontaneous polarization is chosen as the value of charge/area data that corresponds to the time the poling current diminishes, indicating the full poling area has been poled. For the 12kV trial, $P_s$ is found to be 70.5 $\mu C/cm^2$, and for 11.5 kV, $P_s$ is 63.5 $\mu C/cm^2$. This compares nicely to published values of 72 $\mu C/cm^2$. [26, 27, 29]

## 3.2 1D Microfluidic PnC Device

With the electropoling setup fully completed and tested, the PnC fabrication can be performed. Prior to microfluidic experimentation, initial fabrication must be performed and the resulting devices must be studied in order to understand how certain fabrication parameters affect the PnC pattern and bandgap structure. 1D Phononic

crystal chips were designed following the simulation results in Section 2.2.1. The design parameters of the PnC device substrate are a lattice constant of 97.89 μm and a single IDT with a resonance of 43 MHz and an aperture of 1 mm. The microfluidic device that is bonded to the substrate has a width of 400 μm and length of 7 mm. The completed microfluidic device is shown in Figure 3.2.

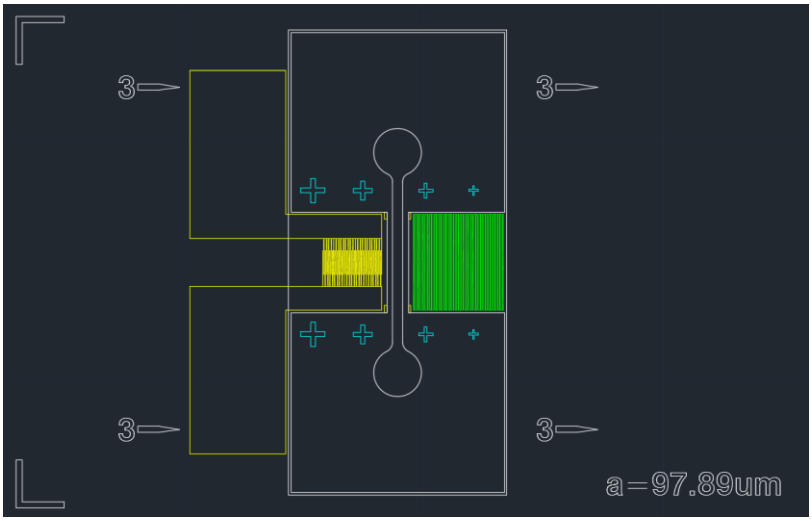


**Figure 3.2:** CAD file of microfluidic PnC device. Yellow figure is the IDT, blue outlines the alignment markers, green outlines the PnC pattern, and white outlines the microfluidic channel.

## 3.2.1 Electropoling Fabrication

PnC devices were fabricated using the electropoling setup and the results are studied to enable fabrication repeatability. A key component to successfully fabricating the phononic crystal is to characterize the poling process and choose an appropriate poling time. When fabricating our first set of 1D PnCs, we applied a long pulse of 2 seconds to see the full poling process. These results are shown in Figure 3.3

(a). As can be seen, the voltage remains constant near 10.5 kV for 540 ms during *t1* before rising up to 11.5 kV, where it remains constant for *t2*. During *t1*, the domains are reversed in the area not covered by photoresist, so the crystal is sufficiently poled after this period. During *t2*, the area under the photoresist tends to be poled, causing the domain inverted regions to become larger than desired. This phenomena is called overpoling, and crystal domains beyond the photoresist boundaries begin to reverse. Long periods of overpoling can cause visible damage to the substrate, as seen in Figure 3.4(c). For successful poling, we want to end the voltage at the end of the *t2* region. Therefore, we select a poling time that just completes the poling process. For our purposes, 700 ms yielded good device results. This poling process is shown in Figure 3.3 (b). The poling process for this crystal is much shorter than the blank crystal, which is consistent to our equations in Section 1.4 which shows the necessary poling charge is proportional to the area. The PnC region less than 1/10 of the blank crystal area.

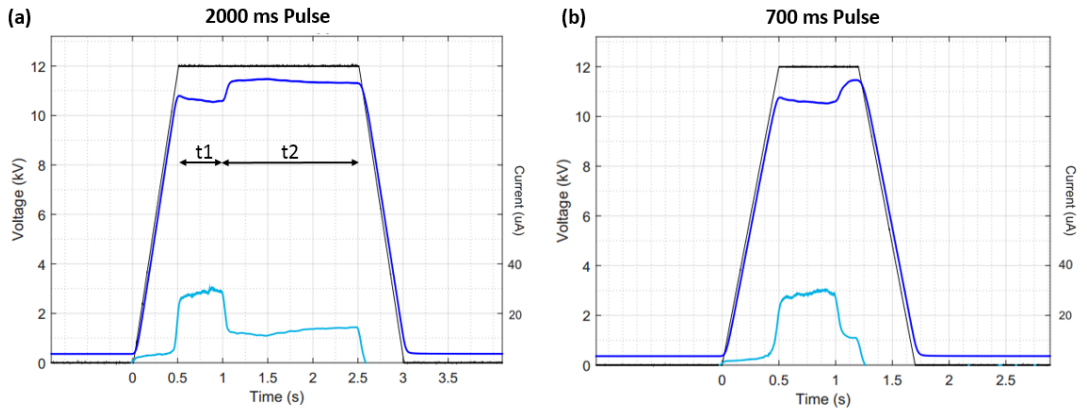


**Figure 3.3** (a) Two second pulse applied to 1D PnC region to characterize the poling time. The t1 region is the period in which the exposed PnC area is being poled, which lasts 540 ms, while t2 indicates the over poling of the crystal (b) 700 ms pulse that was chosen to use for fabrication of 2D PnC devices, which poles the crystal just beyond t1.

We can then observe the poling area under a reflection microscope, due to the differing refractive indexes of the +z and –z domain regions. Figure 3.3(a) shows the 1D crystal with photoresist applied, with the exposed regions having a width of 55 μm. Figure 3.4(b) shows the crystal after 1200 ms of poling, causing the domain width to increase to 66 μm due to overpoling.

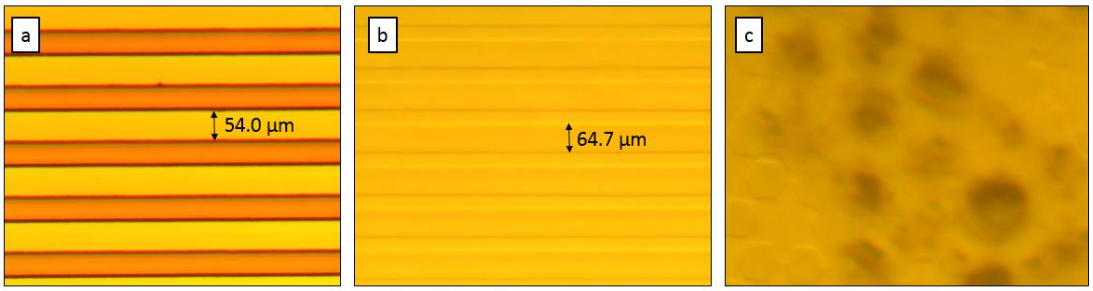


**Figure 3.4**: (a) PnC region covered with photoresist, the exposed areas will be poled while the covered regions should maintain their original polarity. The exposed region is 54.0 μm, while the covered region is 45 μm. (b) The area after the crystal undergoes electropoling. The poled region is 64.7 μm, and the unpoled region is 35.2 μm, indicating obvious overpoling of this domain. (c) Damage to PnC as a result of overpoling. This overpoled device is a 2D PnC.

## 3.2.2 Bandgap Characterization

An important step to developing our technology is experimental characterization of the phononic bandgap to compare our devices to their theoretical behavior, which is done using a slanted IDT configuration. As described in Section 2.2, one dimensional PnCs are fabricated with the above electropoling technique, and slanted IDTs are deposited to each side which have a wideband signal from 30 to 50 MHz. The same is done to a reference device with no PnC region. The transmission

data is shown in Figure 3.5 (a), the cyan line showing the transmission of the reference device and the dark blue showing the PnC device. We can observe a sharp dip in transmission at 40.8 MHz with a bandwidth of about 1.5 MHz, and a strong disruption in transmission between 43 and 46 MHz compared to the reference device. These regions are likely caused by rejection of the frequency bands by the PnC region. The normalized transmission is shown in Figure 3.5(b), illustrating the strong dips in SAW transmission.

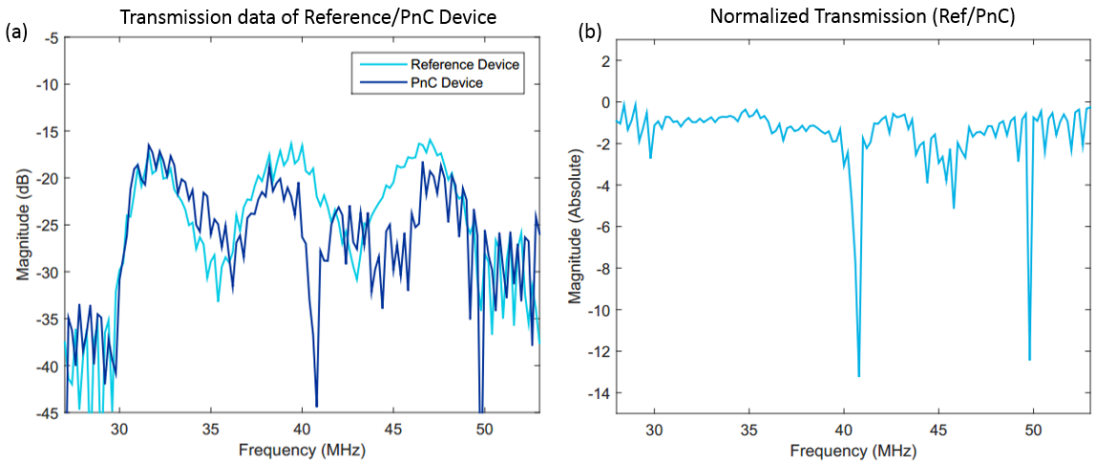


**Figure 3.5**: Characterization of 1D PnC device. The reference device is shown in cyan, which consists of a SAW device with no PnC. The PnC transmission is shown in blue, with strong dips at 40.8 MHz and around 45 MHz. (b) The normalized transmission of the device, indicating strong dips at 40.8 , 45, and 50 MHz. This 50 MHz dip is not obvious in figure (a) but could possibly be the result of a noisy signal or a small band in the higher frequency region.

When comparing these results to those of the simulated bandgap shown in Figure 2.5, there is not exact correlation in terms of frequency, which indicates a 4 MHz bandgap centered at 37 MHz. Our measured bandgap is higher in frequency, near 41 MHz. This is likely due to our fabrication, which usually yields domain sizes that are larger than that of the designed structure, which can cause imperfections in the band structure. However, we are able to identify attenuation of SAW waves in the frequency range we are interested in. This indicates that we are indeed able to fabricate PnCs that can be used to reflect SAW waves, which will add the necessary functionality to integrate PnC-microfluidic technology and study the resulting SSAW field.

### 3.2.3 1D PnC Microfluidic Experiments

To demonstrate the creation of the SSAW pattern in the fluidic channel, we perform controlled experiments on three different devices: device a, which has a single IDT and a PnC region to create a SSAW field; device b, which has a single IDT and no PnC regions, which should perform as a negative control that does not generate a SSAW field; device c, which has a double IDT and no phononic crystal, which is designed to create a SSAW field within the channel at the frequency of 43 MHz. These devices are depicted in Figure 3.6 (a), (b), and (c), respectively. The reflection (blue) and transmission (black) parameters for these devices are also shown in Figure 3.6 (d), (e), and (c). Device (c) is the only device with transmission data, as two IDT pairs are required for this measurement. As can be seen in Figure 3.6(e), there is a small peak around 43 MHz which is not apparent in the non-IDT device shown in Figure 3.6(f). It is possible that this peak is due to reflection of the SAW waves by the PnC.

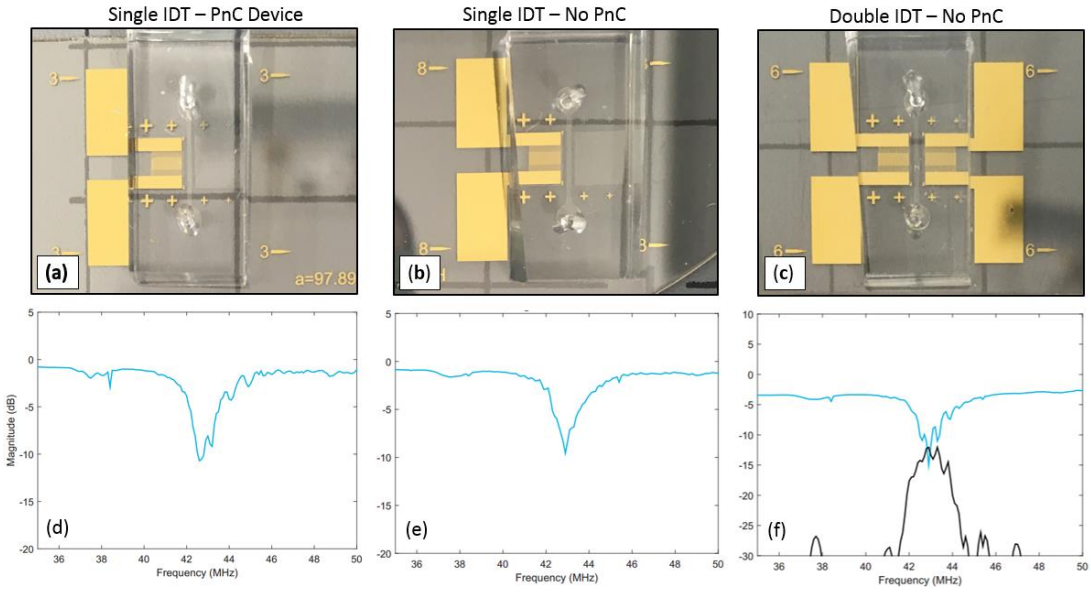


**Figure 3.6** - (a) Single IDT device with PnC region. (b) SIngle IDT device with no PnC region. (c) Double IDT device. (d) reflection data for device a, with a strong dip at 42.7MHz of -10.7 dB and small peak at 43 MHz, potentially indicating the phononic bandgap. (e) Reflection data for device b with a strong dip at 42.9 of -9.57 dB. (f) Reflection and dransmission data of double IDT device, indicating power between the IDTs is strongly trasmitted between 41 and 45 MHz. The strongest reflection dip is at 42.9 MHz with -15.04 dB.

Particle focusing experiments were performed on each device to observe the particle behavior under the SAW field created by each device. 2.2 μm florescent polystyrene beads in 0.1% BSA solution was pumped through the channel at 0.46 μL/min. The IDT was excited with the RF generator, and the device was observed with a Ti-E microscope. Observations were done on device (a). Initially particles were pumped without any RF power applied to the IDT. Particles travelled through the channel in random trajectories with no organization whatsoever as expected. Once power from the RF generator was applied at 43MHz, particles immediately move

laterally towards pressure nodes in the channel and continue through the channel along these trajectories. This indicates that SAWs are being reflected by the PnC region and interacting with the transmitted SAWs, creating a SSAW field which manipulates the movement of the particles.

Interestingly, this frequency does not generate perfect node lines. The particles tend to wiggle through the channel in non-straight node paths. To further study this behavior, we adjust the frequency between 36 MHz and 45 MHz to observe the effect on the SSAW field. Note that while the IDTs have a resonance frequency at 43 MHz, the other frequencies can still excite the IDTs, but there is a weaker coupling of electrical and mechanical energy. We begin at 36 MHz, where particles exhibit very weak organization along node lines, indicating minimal interaction between the PnC and the SAWs. Once we apply 38 MHz, we see a very interesting phenomenon: particles strongly organize along node lines, as well as get pushed to the crystal surface of the device, causing them to drag along the surface as they move through the channel. This indicates there is a strong interaction between the SAWs and the PnC, generating a strong SSAW that has a force component towards bottom of the channel. This interaction seems to lessen once we deviate from 38 MHz, and at 41.5 MHz, the node lines become very weak again, indicating a break in the bandgap. Once we apply the resonant frequency of 42.7 MHz, the beads do move along pressure nodes, but tend to move in a trajectory is not exactly straight but curvy, making the particles appear to wiggle through the channel. Applying 44.5 MHz generates straight node lines with no aberrations in the node trajectory, suggesting this is the frequency in which the PnC

operates the strongest. Seven node lines are observed at 44.5 MHz. Once the frequency nears 45 MHz, the node lines tend to lose their clarity as the SSAW field weakens. Snapshots of these results are shown in Figure 3.7.

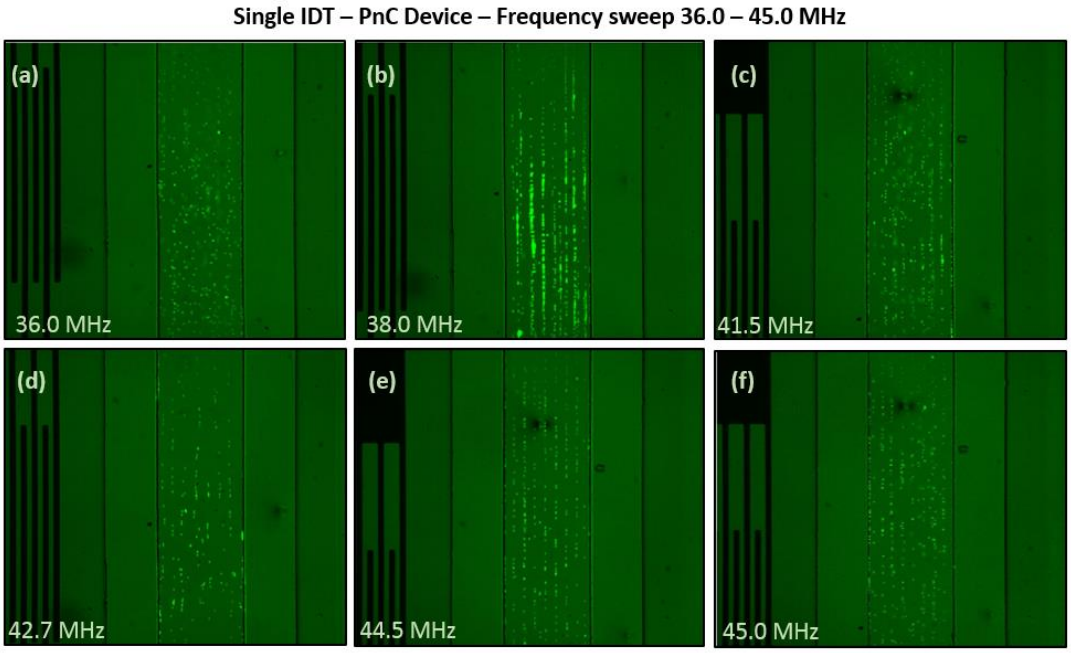


**Figure 3.7**: Microfluidic results of the PnC device when frequency is swept between 36-45 MHz. (a) 36 MHz, pressure nodes are extremely weak, minimal movement of particles towards pressure nodes. (b) 38 MHz, particles are strongly pushed towards node lines, as well as pushed downwards in the channel, causing particles to move across the substrate as they propagate through the channel. (c) 41.5 MHz, SSAW field is much weaker than at 38 MHz creating node lines but not strong node lines, indicating not all SAW energy is being reflected by PnC. (d) 42.7 MHz, near the resonant frequency of the IDT. Particles move long node lines, but tend to move in non-straight trajectories, causing particles to "wiggle" through the channel. (e) 44.5 MHz, very straight, strong node lines, indicating strong SSAW field due to strong rejection of SAWs by the PnC. This is the most ideal SSAW field generated in this experiment. (f) 45 MHz, noticeable attenuation of SSAW strength as PnC becomes permeable to SAWs in the frequency.

Strong node lines are seen both at 38 MHz and 44.5 MHz. When comparing to the bandgap characterization results in Figure 3.4, we have both agreement and disagreement. Both indicate bandgaps in two respective frequency ranges, but unfortunately there is a difference in poling times between the characterized PnC and the microfluidic PnC, which likely resulted in different bandgaps. The characterization data shows attenuation at 41 MHz and between 43 and 46 MHz. This matches the microfluidic SAW reflection at 44.5 MHz, but not at 38MHz. It is possible that the characterization bandgap at 41 MHz is shifted down to 38 MHz in the microfluidic device. Further characterization experiments are required to fully understand this mismatch.

While work still must be done to have full agreement between characterization and microfluidic experiments, it is still clear that certain bands of SAW frequencies are being reflected back to create a standing acoustic pattern within the channel. Such behavior indicates coherent transmission of the acoustic power, a powerful observation of the reflective nature of phononic crystals. Indeed, this provides an important understanding of phononic crystals, enabling strong control of the phase information of the reflected wave which will be useful both in future studies of phononic crystals and their applications.

To ensure this behavior is due to the phononic nature of the crystal, we next observe the behavior of the single IDT without phononic crystal under the same conditions. Beads in the channel flow with no organization when power is off. Application of power at 43 MHz causes no visible shift in bead trajectory, and no

acoustic nodes are observable. Again, the input is varied between 36 and 45 MHz, which yields no change in particle movement. These results are shown in Figure3.6(c) and (d). This indicates that without the phononic crystal, all energy is transmitted and none is reflected, resulting in no SSAW field. As such, the beads are subjected to only a TSAW field of much less amplitude. We may suspect that even a TSAW field would push the beads laterally across the channel away from the IDT. Going back to section 1.3.3 we see that given our device parameters, our κ value is given by $\kappa = \frac{\pi f_{TSAW} d_p}{c_f}$, and given a TSAW frequency of 43 MHz, particle diameter of 2.2 μm, and fluidic velocity of 1450 m/s, we yield a κ value of 0.205. To observe a noticeable TSAW effect on the particles, we would need to have κ slightly larger than 1. Therefore this observed behavior is expected and reveals negligible reflection of reflected SAW energy.

Lastly we observe the behavior of device (c) to provide results of a perfect SSAW field as reference for our PnC device. An input of 44.5 MHz causes the particles immediately shift position towards the nearest node line. Particles continue down this node line for duration of the channel. Seven very straight node lines are observed, the same amount observed by the PnC device at 44.5 MHz. The results of this trial are shown in Figure 3.8 (e) and (f). Again the frequency was swept and orderly node lines were observed between 38 and 44.5 MHz. Outside this range the particles tended to move disorderly as the SSAW field became weak and eventually non-existent. Particles were again subjected to a SSAW field that pushed them towards the surface

at 38 MHz, just as the PnC device. After this frequency, node lines were detected up until about 45 MHz, with 44.5 yielding the best SSAW pattern. Similar to the PnC device, the 44.5 MHz SSAW field appeared stronger than that generated at 43 MHz, which appeared more disorganized due to weaker SSAW forces.

This correlation in behavior of the PnC device and double IDT device demonstrates that the SSAW field generated by the PnC device strongly resemble that created by the perfect reference. The absence of SSAW fields in certain frequency bands indicates the frequency dependent nature of the PnC bandgap, rejecting SAWs of certain frequencies while others are able to transmit.

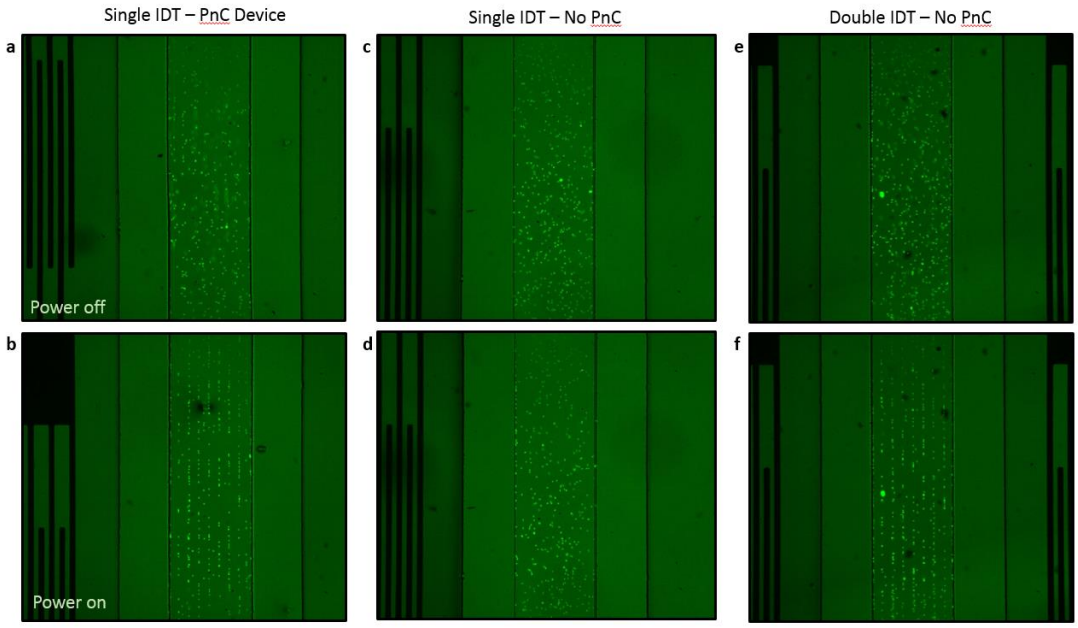


**Figure 3.8** - (a) PnC Device channel with no RF power. (b) PnC Channel with RF power at 44.5 MHz. 7 strong node lines are observed, indicating a well formed SSAW field. (c) Channel of negative control device without applied power. (d) Power applied to negative control device at 44.5 MHz, resulting in no node lines or particle manipulation in channel. (e) Double IDT device without power applied. (f) 44.5 MHz signal, creating strong node lines, offering a reference to our PnC device.

## 3.3 2D Microfluidic PnC Device

Our 1D microfluidic results laid out a blue print for us to further our devices and expand them to a two-dimensional geometry. This geometry is more robust, as a two-dimensional crystal should be able to reflect both acoustic waves that are normal to the PnC region, as well as those that hit at an angle. With strong SSAW fields at 38 MHz and 44.5 MHz, we decided to focus our 2D PnC devices to replicate and enhanced the SSAW field at 38 MHz, as the forcing of beads to the crystal surface opens up potential integration with other SAW mechanics for future microfluidic PnC devices.

With the development of a characterization scheme to study PnC transmission and functional microfluidic PnC fabrication process, we have the tools to be able to further our studies to the 2D device. We begin by choosing a PnC design which should have a bandgap approximately around 38 MHz. We used COMSOL simulations to find the approximate region of the bandgap, and then used transmission data to characterize the bandgap. The 2D PnC design used has a honeycomb lattice pattern with hexagonal inclusions as shown in Figure 2.6 (a). We focus on a design a 110 μm periodicity and hexagons with a sidelength of 20 μm.

### 3.3.1 Bandgap dependence on Poling Time

The first studies of the 2D PnC device included characterizing the phononic bandgap for different poling times during PnC fabrication. This PnC region consisted of 23 periods of the honeycomb lattice, and had an exposed area of 3.12 $mm^2$. Initial

studies showed us that the PnC completes poling at about 400 ms. Therefore, we apply voltage for 600 ms, 1000 ms, and 1400 ms. Poling for shorter time periods tended to yield PnCs that were missing hexagonal inclusions, indicating the poling process was not completed. The poling stage and PnC patterns are shown in Figure 3.9.

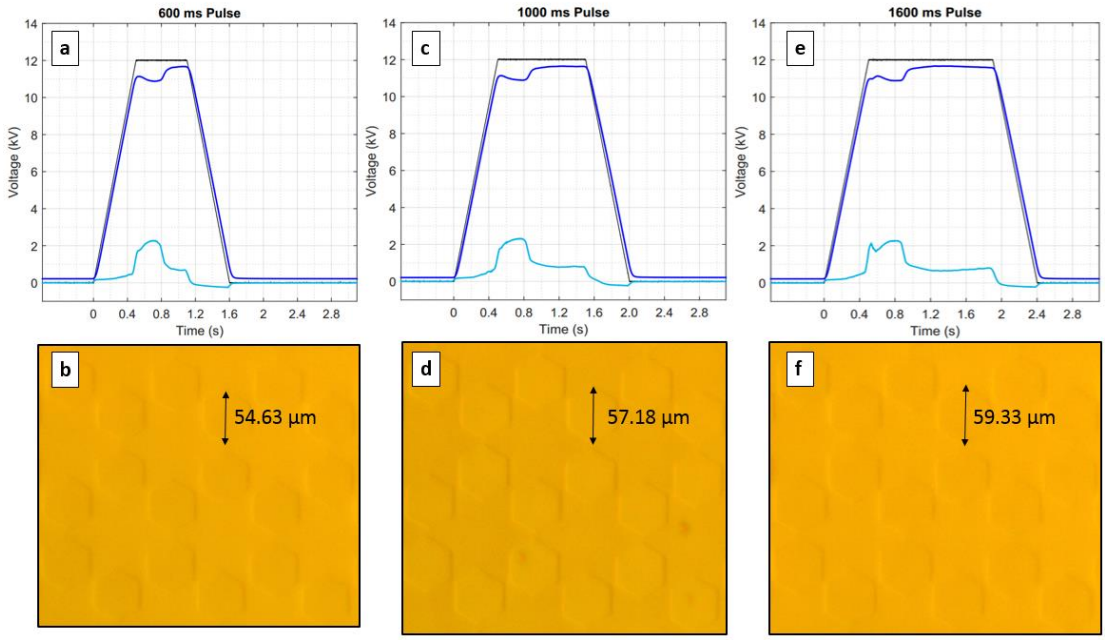


**Figure 3.9:** Electropoling and hexagonal data from PnC with 23 periods and a diameter of 40 µm. (a) 600 ms poling stage, including 344 ms of poling and 255 of overpoling. (b) resulting hexagonal lattice, which has a diameter of 14.63 µm than designed. (c) 1000 ms poling stage, including 362 ms of poling and 630 ms of overpoling. (d) Resulting hexagonal lattice, with diameter increasing 2.55 µm from the previous trial. (e) 1400 ms poling stage, including 411 ms of poling and 980 ms of overpoling. (f) Resulting hexagonal lattice, with diameter increasing 2.15 µm from the previous trial.

As we can see, the hexagonal inclusions are much larger than the designed 40 μm diameter. For a smaller diameter, we can either change our design or lessen our poling time. However, since lower poling times tend to yield imperfect PnC regions, changing the design will likely give us our desired diameter. According to simulations, the diameter of the hexagons does not significantly change the location of the bandgap, but does increase the bandwidth of the bandgap, meaning these larger hexagons are likely advantageous.

With our slanted IDT characterization scheme, we measure the transmission of the above PnCs. The results are shown in Figure 3.10.

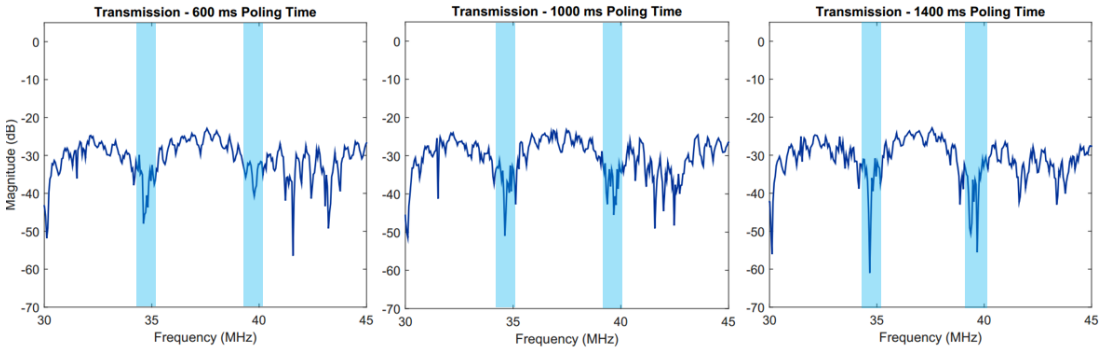


**Figure 3.10:** Transmission data identifying bandgaps at 34.7 and 39.8 MHz. Increasing poling time results in stronger attenuation of these frequency bands.

We can see from these results that two bandgaps remain at the same frequency for each crystal, 34.7 MHz and 39.8 MHz. As the poling time increases, the acoustic attenuation tends to decrease. The 34.7 MHz bandgap has a signal of -48.0 dB, -50.9 dB, and -61.0 dB with increasing poling time, while the 39.8 MHz bandgap's signal strength

decreases as -40.7 dB, -45.5 dB, and -55.6 dB. This data shows how acoustic attenuation can be enhanced with longer poling time. While this is favorable, we must note that very long poling times will result in overpoling defects, as depicted in Figure 3.3(c). Our 1400 ms devices did suffer from slight overpoling defects that were located outside of the PnC region, meaning that longer poling time could cause overpoling defects that will damage the effectiveness of the PnC. At this point, it is uncertain if this bandgap rejection improvement is due to increased domain reversal depth or hexagon diameter.

### 3.3.2 Bandgap dependence on PnC area

We further study the 2D PnC bandgap decreasing the amount of periods of the PnC lattice so that we can identify how many periods are required to make a device with an adequate amount of acoustic rejection to make a successful microfluidic device. Shrinking the size of the PnC region will make the PnC take less room on the chip, which can be used to add other SAW based components to the chip for further manipulation capabilities. To conduct this study, we fabricated devices with 5 periods, 10 periods, and 23 periods with lattice parameters described in the previous section. The time was adjusted to meet the requirements of the PnC area, using 1400 ms for the 23 period device as a reference. The characterization results are shown in Figure 3.11

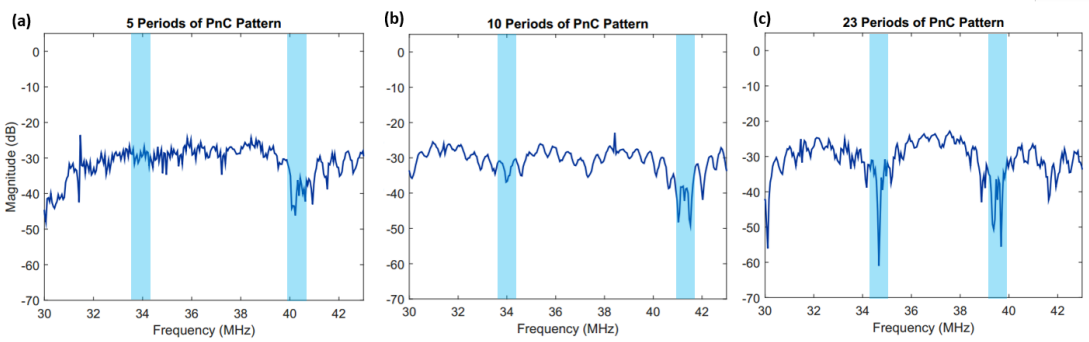


**Figure 3.11**: Transmission data from devices with an increasing number of lattice periods, which indicate that bandgaps centered near 34 MHz and 40 MHz attenuate more greatly as more periods are added to the device. The 5 period PnC likely exhibits a band at 34 MHz, but it is too weak to attenuate the SAWs at this frequency.

We can see a trend of increased attenuation of acoustic power with increasing amount of lattice periods. Figure 3.11 suggest that there is a bandgap near 40 MHz that causes greater acoustic attenuation as the amount of periods increases, well as a bandgap near 34 MHz that becomes significantly more apparent with a greater amount of periods. The 5 period device only has a strong transmission dip at 40.2 MHz, with a magnitude of -46.2 dB. This device likely has an additional bandgap at 34 MHz, but is too weak to create a significant attenuation in the transmission data. The 10 period device exhibits a strong attenuation dip centered at 41.2 MHz with a signal of -49.14 dB, very close to the bandgap location of the 5 period device. It also has smaller dips at 34 MHz (-36 dB) and 37.3 MHz (-36 dB). Lastly the 23 period PnC exhibits a strong dip at 39.7 MHz with a signal of -55.6 dB, as well as at 34.7 with a signal of -61dB.

These three trials demonstrate that transmission near 34 MHz and 40 MHz is more greatly attenuated as the number of lattice periods increases, indicating that the

phononic bandgaps reject phonons more effectively. This type of experiment is useful in PnC design to determine how many lattice periods are required to effectively reject the SAW frequency of interest. While adding more periods caused greater attenuation, the 5 period device does indeed attenuate 40.2 MHz quite well, and could be quite useful for a device with a smaller footprint. By further studying the bandgap dependence on lattice periods, we can gain further control in SAW rejection to create more useful microfluidic PnC devices.

### 3.3.3 2D PnC Microfluidic Experiment

Microfluidic particle focusing experiments are performed on a 2D microfluidic PnC device. This device has a similar layout to that of Figure 3.5, with a few adjustments: the PnC region consists of a 2D geometry, the IDT is designed to operate at 38 MHz in order to apply more acoustic power to the SSAW mode that exerts a downward force on the particles, and the channel width is changed to 300 μm. The honeycomb lattice has a period of 110 μm, and PnC is composed of 10 periods. The device is a fabricated with our standard procedure and is poled for 300 ms. The fabrication procedure was not optimized at the point of this experiment, and these results offer a proof-of-concept device operation.

The chip is placed under a microscope and beads are pumped into the channel at 0.4 uL/min. Initially the particles travel through the channel in disorganized trajectories. The IDT is then stimulated at 38 MHz, and particles immediately move towards node lines, indicating the generation of a SSAW field. Within a few seconds

it is apparent that the particles are moved onto the surface, as their velocity through the channel significantly decreases as they are subjected to the SSAW field. Snapshots from this experiment are shown in Figure 3.12.

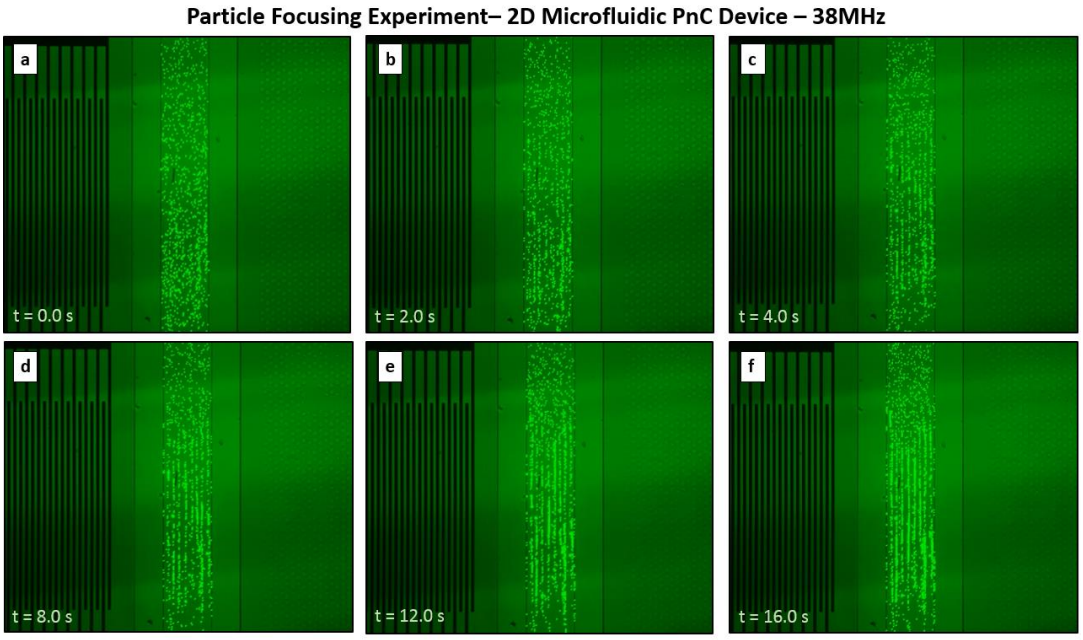


**Figure 3.12:** Temporal results of 2D Microfluidic PnC operating at 38 MHz. (a) No SAW has been applied. (b) The SSAW field has been turned on and particles begin to move towards node lines. (c) Node lines are enhanced. (d-f) Progression shows how the particles are pushed towards the substrate as the SSAW field acts on them. They tend to slow down and "crawl" along the substrate, causing strands of node lines to build up as more and more particles move through the channel and get stuck on the substrate.

These results demonstrate that we were able to successfully reflect the 38 MHz SAW with our 2D PnC device, and able to replicate the SSAW field that creates a downward force on the particles that pushes them towards the substrate. When varying the input frequency of this device, we found that the SSAW field diminished quickly as we deviated from 38 MHz, while finding particle focusing modes at 33MHz, and 42 MHz, indicating additional frequency bands at were rejected by this PnC.

The location bandgaps that are measured by the microfluidic experiment and the bandgap characterization of a 10 period device match excellently. The microfluidic results demonstrate bandgaps at 33, 38, and 42 MHz, while the characterization data shows dips at 34, 37.3, 41.2 MHz (Figure 3.11(b)). The locations are therefore very nearby, only deviating at most 1 MHz from each other. This agreement is the first concrete connection made between characterization and microfluidic experimentation, and will set the stage for further studies of our microfluidic PnC device development. Such good correlation was certainly made possible by careful experimental planning that allowed us to grow our knowledge foundation incrementally, as shown in the previous experimental results presented in this paper.

Laying out the device blueprint with the 1D devices allowed us to develop our fabrication and characterization methods with a relatively straightforward PnC geometry, which we could easily expand towards our 2D design. Further optimization will allow us to gain a strong control over the location and strength of the PnC bandgap in order to maximize this node finding behavior. This way we can develop a strong foundation to use this PnC based SAW reflection and tune it to our specific application.

# Chapter 4: Conclusion

We have successfully integrated two very large fields, phononic crystals and acoustic microfluidics, on a single chip. In doing so we were able to demonstrate coherent reflection of acoustic waves resulting from the interaction of SAW waves with a phononic crystal region, and observing the SAW field manipulate particles within the microfluidic channel. We designed, built, and tested an experimental setup to perform electropoling in order to create phononic crystals that varied in their piezoelectric domain directions. In doing so, we were able to fabricate topographically monolithic crystals. Simulations were done in order to theoretically explore the bandgap. We developed a fabrication scheme to fabricate phononic crystals onto a $LiNbO_3$ substrate and then apply IDTs at the correction position with respect to the phononic crystal region. Wideband IDTs were used to experimentally characterize the PnC bandgap, which was compared to the simulated bandgap. While the experimental and theoretical bandgaps did not completely correlate, the experimental bandgap matched well to our microfluidic results.

Microfluidic devices has become a booming research field since its initial studies. Novel geometries have enhanced the functionality of biological SAW devices in strong ways. With phononic crystals becoming more feasible to fabricate, it appears possible that phononic integration becomes a more heavily used component in microfluidic devices to enable a new methods of manipulation. Phononic crystal microfluidics need not be confined to only acoustic reflection, but also can be used to

focus acoustic energy to create a stronger SAW force density, acoustic waveguides to allow SAWs to only act in a small region of the channel, and acoustic cavities to create small regions where acoustic energy gets trapped.

Indeed phononic crystals enable a new degree of control in acoustic manipulation. However, this research area has been minimally explored. Our design has demonstrated acoustic reflection, but new geometries can enable manipulation beyond. A key component that this design did not explore is the frequency dependence of phononic crystals which could bring particle manipulation to a point not yet seen with current microfluidic technology. Because phononic crystals can only interact SAWs at specific frequencies, other frequencies propagate through the PnC with minimal attenuation. Therefore, phononic crystals with different operational frequencies can be placed at a single chip, each used to enable a different type of acoustic manipulation without interfering with each other. Exploitation of the acoustic frequency for microfluidic functionality has not been explored but could be a very fruitful endeavor, enabling microfluidic functionality currently unseen in current acoustofluidic chips. However, I believe it is a very attainable field that can hopefully be explored with further efforts in the integration with phononic crystal with microfluidic devices.

# References

[1] Achaoui, Y., Khelif, A., Benchabane, S., Robert, L. and Laude, V., 2011. Experimental observation of locally-resonant and Bragg band gaps for surface guided waves in a phononic crystal of pillars. *Physical Review B*, *83*(10), p.104201.

[2] Achaoui, Y., Laude, V., Benchabane, S. and Khelif, A., 2013. Local resonances in phononic crystals and in random arrangements of pillars on a surface. *Journal of Applied Physics*, *114*(10), p.104503.

[3] Ash, B. J., et al. "A highly attenuating and frequency tailorable annular hole phononic crystal for surface acoustic waves." *Nature Communications* 8.1 (2017): 174.

[4] Ballantine Jr, D. S., Robert M. White, Stephen J. Martin, Antonio J. Ricco, E. T. Zellers, G. C. Frye, and H. Wohltjen. *Acoustic wave sensors: theory, design and physico-chemical applications*. Academic press, 1996.

[5] Benchabane, S., Gaiffe, O., Salut, R., Ulliac, G., Laude, V. and Kokkonen, K., 2015. Guidance of surface waves in a micron-scale phononic crystal line-defect waveguide. *Applied Physics Letters*, *106*(8), p.081903.

[6] Benchabane, S., Khelif, A., Rauch, J.Y., Robert, L. and Laude, V., 2006. Evidence for complete surface wave band gap in a piezoelectric phononic crystal. *Physical Review E*, *73*(6), p.065601.

[7] Bogomolov, V.N., Gaponenko, S.V., Germanenko, I.N., Kapitonov, A.M., Petrov, E.P., Gaponenko, N.V., Prokofiev, A.V., Ponyavina, A.N., Silvanovich, N.I. and Samoilovich, S.M., 1997. Photonic band gap phenomenon and optical properties of artificial opals. Physical Review E, 55(6), p.7619.

[8] Chezganov, D.S., Vlasov, E.O., Gimadeeva, L.V., Alikin, D.O., Chuvakova, M.A., Vaskina, E.M. and Shur, V.Y., 2017. Growth of isolated domains induced by focused ion beam irradiation in congruent lithium niobate. *Ferroelectrics*, *508*(1), pp.16-25.

[9] Collins, D.J., Ma, Z., Han, J. and Ai, Y., 2017. Continuous micro-vortex-based nanoparticle manipulation via focused surface acoustic waves. *Lab on a Chip*, *17*(1), pp.91-103.

[10] Destgeer, G., Ha, B.H., Jung, J.H. and Sung, H.J., 2014. Submicron separation of microspheres via travelling surface acoustic waves. *Lab on a Chip*, *14*(24), pp.4665-4672.

[11] Destgeer, G., Jung, J.H., Park, J., Ahmed, H., Park, K., Ahmad, R. and Sung, H.J., 2017. Acoustic impedance-based manipulation of elastic microspheres using travelling surface acoustic waves. *RSC Advances*, *7*(36), pp.22524-22530.

[12] Destgeer, G. and Sung, H.J., 2015. Recent advances in microfluidic actuation and micro-object manipulation via surface acoustic waves. *Lab on a Chip*, *15*(13), pp.2722-2738.

[13] Ding, X., Li, P., Lin, S.C.S., Stratton, Z.S., Nama, N., Guo, F., Slotcavage, D., Mao, X., Shi, J., Costanzo, F. and Huang, T.J., 2013. Surface acoustic wave microfluidics. *Lab on a Chip*, *13*(18), pp.3626-3649.

[14] Eichenfield, M., Chan, J., Camacho, R.M., Vahala, K.J. and Painter, O., 2009. Optomechanical crystals. *Nature*, *462*(7269), pp.78-82.

[15] Franke, T., Abate, A.R., Weitz, D.A. and Wixforth, A., 2009. Surface acoustic wave (SAW) directed droplet flow in microfluidics for PDMS devices. *Lab on a Chip*, *9*(18), pp.2625-2627.

[16] Gorishnyy, T., Maldovan, M., Ullal, C. and Thomas, E., 2005. Sound ideas. *Physics World*, *18*(12), p.24.

[17] Gorishnyy, T., Ullal, C.K., Maldovan, M., Fytas, G. and Thomas, E.L., 2005. Hypersonic phononic crystals. *Physical review letters*, *94*(11), p.115501.

[18] Hopkins, P.E., Reinke, C.M., Su, M.F., Olsson III, R.H., Shaner, E.A., Leseman, Z.C., Serrano, J.R., Phinney, L.M. and El-Kady, I., 2010. Reduction in the thermal conductivity of single crystalline silicon by phononic crystal patterning. *Nano letters*, *11*(1), pp.107-112.

[19] Huang, C.P. and Zhu, Y.Y., 2005. Piezoelectric-induced polariton coupling in a superlattice. *Physical review letters*, *94*(11), p.117401.

[20] Huang, C.P. and Zhu, Y.Y., 2012. Piezoelectric superlattice: From piezoelectric to Huang-Kun-like equations. *AIP Advances*, *2*(4), p.042117

[21] Khelif, A., Achaoui, Y., Benchabane, S., Laude, V. and Aoubiza, B., 2010. Locally resonant surface acoustic wave band gaps in a two-dimensional phononic crystal of pillars on a surface. *Physical Review B*, *81*(21), p.214303

[22] Länge, K., Rapp, B.E. and Rapp, M., 2008. Surface acoustic wave biosensors: a review. *Analytical and bioanalytical chemistry*, *391*(5), pp.1509-1519.

[23] Laude, V., Wilm, M., Benchabane, S. and Khelif, A., 2005. Full band gap for surface acoustic waves in a piezoelectric phononic crystal. *Physical Review E*, *71*(3), p.036607.

[24] Lin, C.M., Chen, Y.Y. and Wu, T.T., 2006. A novel weighted method for layered SAW filters using slanted finger interdigital transducers. *Journal of Physics D: Applied Physics*, *39*(3), p.466.

[25] Maldovan, M., 2013. Sound and heat revolutions in phononics. *Nature*, *503*(7475), pp.209-217.

[26] Miller, G.D., 1998. *Periodically poled lithium niobate: modeling, fabrication, and nonlinear-optical performance*(Doctoral dissertation, Stanford University)

[27] Min-Ji, J., Oc-Yeub, J., Byeong-Joo, K. and Myoungsik, C., 2005. Fabrication of periodically poled lithium niobate crystal and poling-quality evaluation by diffraction measurement. *Journal of Korean Physical Society*, *47*, p.336.

[28] Minnich, A., Dresselhaus, M.S., Ren, Z.F. and Chen, G., 2009. Bulk nanostructured thermoelectric materials: current research and future prospects. *Energy & Environmental Science*, *2*(5), pp.466-479.

[29] Myers, L.E., Eckardt, R.C., Fejer, M.M., Byer, R.L., Bosenberg, W.R. and Pierce, J.W., 1995. Quasi-phase-matched optical parametric oscillators in bulk periodically poled LiNbO 3. *JOSA B*, *12*(11), pp.2102-2116.

[30] Pennec, Y., Rouhani, B.D., Larabi, H., Akjouj, A., Gillet, J.N., Vasseur, J.O. and Thabet, G., 2009. Phonon transport and waveguiding in a phononic crystal made up of cylindrical dots on a thin homogeneous plate. *Physical Review B*, *80*(14), p.144302.

[31] Shi, J., Huang, H., Stratton, Z., Huang, Y. and Huang, T.J., 2009. Continuous particle separation in a microfluidic channel via standing surface acoustic waves (SSAW). *Lab on a Chip*, *9*(23), pp.3354-3359.

[32] Shi, J., Yazdi, S., Lin, S.C.S., Ding, X., Chiang, I.K., Sharp, K. and Huang, T.J., 2011. Three-dimensional continuous particle focusing in a microfluidic channel via standing surface acoustic waves (SSAW). *Lab on a Chip*, *11*(14), pp.2319-2324.

[33] Shi, J., Mao, X., Ahmed, D., Colletti, A. and Huang, T.J., 2008. Focusing microparticles in a microfluidic channel with standing surface acoustic waves (SSAW). *Lab on a Chip*, *8*(2), pp.221-223

[34] Shiokawa, S. and Kondoh, J., 2004. Surface acoustic wave sensors. *Japanese journal of applied physics*, *43*(5S), p.2799.

[35] Shur, V.Y., Rumyantsev, E.L., Batchko, R.G., Miller, G.D., Fejer, M.M. and Byer, R.L., 1999. Domain kinetics in the formation of a periodic domain structure in lithium niobate. *Physics of the solid state*, *41*(10), pp.1681-1687.

[36] Weis, R.S. and Gaylord, T.K., 1985. Lithium niobate: summary of physical properties and crystal structure. *Applied Physics A: Materials Science & Processing*, *37*(4), pp.191-203.

[37] Whitesides, G.M., 2006. The origins and the future of microfluidics. *Nature*, *442*(7101), pp.368-373.

[38] Yu, J.K., Mitrovic, S., Tham, D., Varghese, J. and Heath, J.R., 2010. Reduction of thermal conductivity in phononic nanomesh structures. *Nature nanotechnology*, *5*(10), pp.718-721.

[39] Yudistira, D., Boes, A., Djafari-Rouhani, B., Pennec, Y., Yeo, L.Y., Mitchell, A. and Friend, J.R., 2014. Monolithic phononic crystals with a surface acoustic band gap from surface phonon-polariton coupling. *Physical review letters*, *113*(21), p.215503.

[40] Yudistira, D., Boes, A., Janner, D., Pruneri, V., Friend, J. and Mitchell, A., 2013. Polariton-based band gap and generation of surface acoustic waves in acoustic superlattice lithium niobate. *Journal of Applied Physics*, *114*(5), p.054904.

[41] Yudistira, D., Pennec, Y., Djafari Rouhani, B., Dupont, S. and Laude, V., 2012. Non-radiative complete surface acoustic wave bandgap for finite-depth holey phononic crystal in lithium niobate. *Applied Physics Letters*, *100*(6), p.061912.

[42] Zhang, X.J., Zhu, R.Q., Zhao, J., Chen, Y.F. and Zhu, Y.Y., 2004. Phonon-polariton dispersion and the polariton-based photonic band gap in piezoelectric superlattices. *Physical Review B*, *69*(8), p.085118.

[43] Zhu, Y.Y., Zhang, X.J., Lu, Y.Q., Chen, Y.F., Zhu, S.N. and Ming, N.B., 2003. New type of polariton in a piezoelectric superlattice. *Physical review letters*, *90*(5), p.053903.

[44] Zen, N., Puurtinen, T.A., Isotalo, T.J., Chaudhuri, S. and Maasilta, I.J., 2014. Engineering thermal conductance using a two-dimensional phononic crystal. *Nature communications*, *5*, p.3435.